CHEMISTRY OF MATERIALS

pubs.acs.org/cm

Article

Au Nanobead Chains with Tunable Plasmon Resonance and Intense Optical Scattering: Scalable Green Synthesis, Monte Carlo Assembly Kinetics, Discrete Dipole Approximation Modeling, and Nano-Biophotonic Application

Alan McLean, Michael Kanetidis, Tarun Gogineni, Rahil Ukani, Ryan McLean, Alexander Cooke, Inbal Avinor, Bing Liu, Panos Argyrakis,* Wei Qian,* and Raoul Kopelman*

Cite This: *Chem. Mater.* 2021, 33, 2913−2928

Read Online

ACCESS | Metrics & More | Article Recommendations | Supporting Information

ABSTRACT: The development of optically tunable and intensely scattering materials is of wide interest in biophotonics and medicine, provided they are biocompatible. Highly linear, tunable, narrow-gap, and intensely scattering gold nanobead chains were prepared by a green synthesis scheme, starting from ultrapure gold nanosphere monomers having a virgin surface. These Au nanochains exhibit a tunable longitudinal surface plasmon resonance (SPR) over the range from 590 to 710 nm. To determine the ensemble statistics of the synthesized nanobead chain lengths and their branching, transmission electron microscopy (TEM) images were acquired, in batch, correlated with the nanochain longitudinal SPR maxima (590 to 640 nm). Monte Carlo simulations quantify the selectivity of the chemical reaction: chain-end gold nanosphere units are about 4 times more reactive than chain-center units and assemble under a high-inverse-order-dependent diffusion. Discrete dipole approximation (DDA) computations predict the experimental extinction spectra and the narrow gap distance of the chains, as well as the elongated chain's optical scattering enhancement, relative to Au nanosphere monomers (approximately 3× enhancement at equivalent mass). *In vitro* dark-field microscopy, cell studies, and biocompatibility tests demonstrate the nanochains' (1) intense optical scattering cross sections, related to the plasmon coupling between the constituent nanospheres, (2) highly accessible gold surfaces, enabling facile conjugation with cell targeting ligands, and (3) absence of cell toxicity. The herein reported scalable, green synthesized, readily conjugatable gold nanobead chains are thus of great potential utility for serving as a wide range of biophotonic platforms, such as for enhanced *in vitro* and *in vivo* contrast imaging, diagnostics, and targeted nanotheranostics.

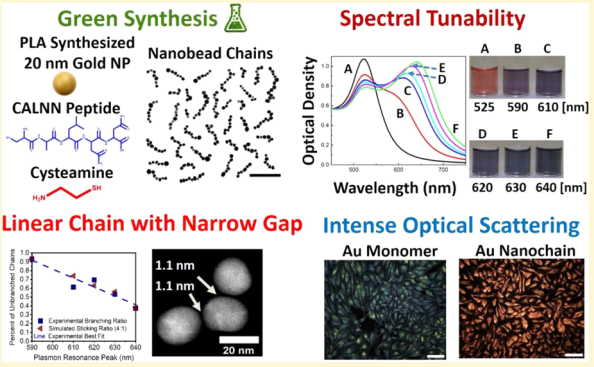

1. INTRODUCTION

Possessing unique size-, morphology-, and composition-dependent optical properties not observed from their bulk or molecular nanocluster counterparts, colloidal gold nanoparticles (Au NPs) have been intensively studied over the last two decades.[1,2] The novel optical properties of these colloidal Au NPs have been attributed to a localized surface plasmon resonance (LSPR) that arises from collective oscillations of the conducting electrons in the valence band.[3,4] Due to their plasmonic optical activity, Au NPs have been utilized in a variety of biomedical applications, including imaging,[5−7] chemical sensing,[8−10] diagnostics,[5,11] and cancer/disease therapies.[11−16] While Au NPs do exhibit extensive biomedical utility, 5−200 nm spherical monomers are optically active only in the range of 520−580 nm, with larger Au NPs exhibiting red-shifted activity.[1,17] Compared to imaging in the visible regime, imaging in the red and near-infrared regimes (600 nm−1000 nm) is more desirable in nanoparticle-assisted biophotonics, because tissue light scattering, cellular background (autofluorescence etc.), and *in vivo* hemoglobin spectral overlap are all highly reduced.[18,19]

Approaches toward fabricating Au NPs that exhibit plasmonic absorption at redder wavelengths involve modifications to the NP monomer, either by lengthening an optical axis of the Au NP ("nanorods")[20] or by synthesizing novel Au morphologies such as Au nanostars, nanoprisms, nanocups, and nanopopcorn.[21−24] Elongated Au nanorods and many novel Au morphologies like nanostars, nanoprisms, and nanocups are typically scalable and easy to produce; however,

Received: January 29, 2021
Revised: March 24, 2021
Published: April 7, 2021

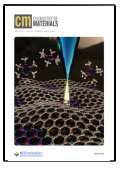

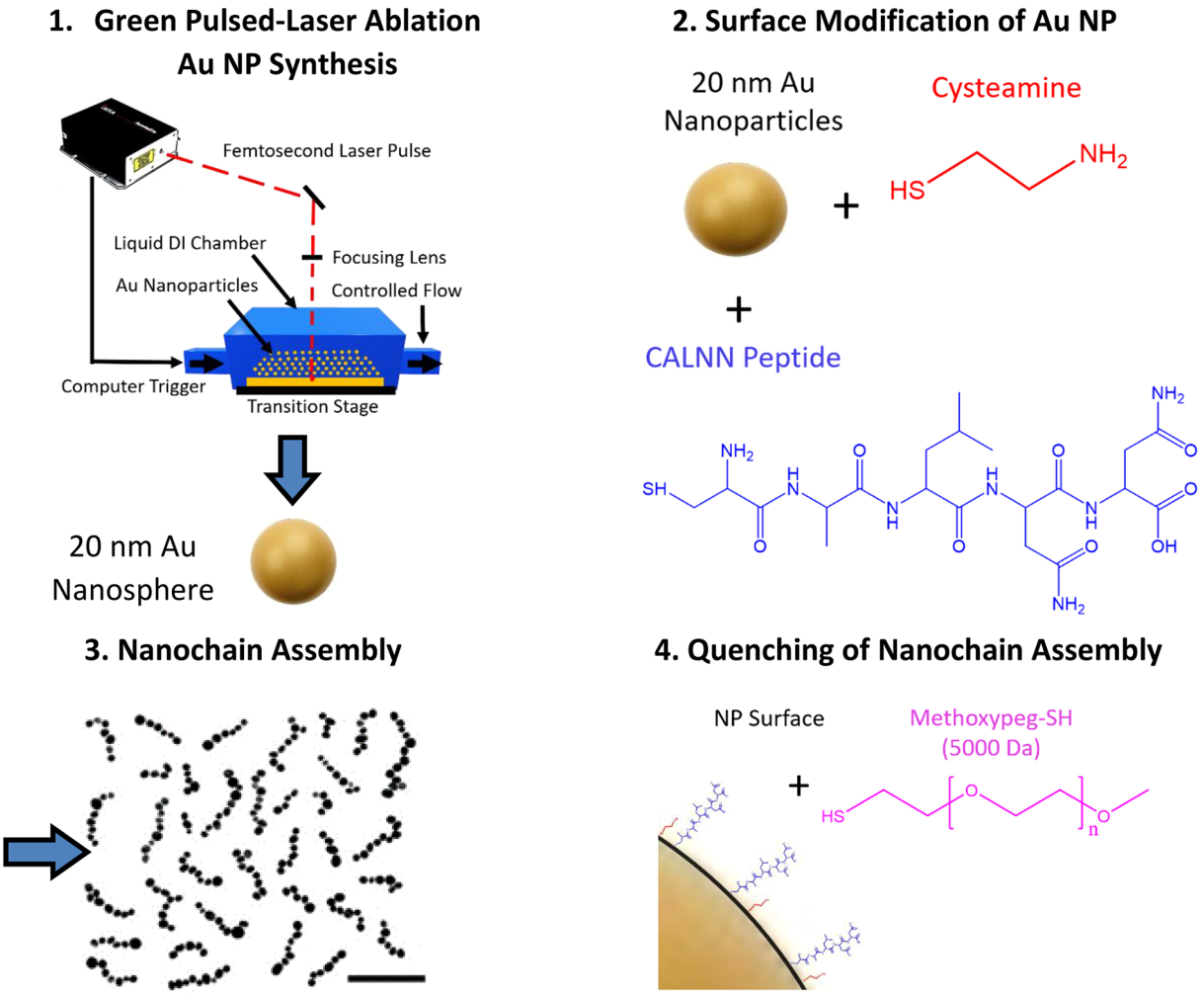

Figure 1. Summary of Au nanochain formation. Step 1. Au NP (nanoparticle) "monomers" of 20 nm in diameter nanospheres, having virgin surfaces, are produced by pulsed laser ablation (PLA). Step 2. Surfaces of monomers are modified with CALNN peptide (blue; 2400:1 relative to Au monomer) and cysteamine (red; 1800:1 relative to Au monomer). Step 3. Self-assembly of Au nanosphere monomers into nanosphere nanochains, after surface modification. The ensemble of nanochains (nanobead chains) having a longitudinal surface plasmon resonance mode at 620 nm is shown as an example (scale bar is 200 nm). Step 4. Nanochain growth is controlled by UV−vis monitoring and quenching at a desired longitudinal SPR, using thiol terminated methoxy poly(ethylene glycol) (mPEG-SH) with a molecular weight of 5000 Da (200:1 relative to Au monomer) that binds to the NP surface.

they suffer as applied biomaterials due to their intrinsic biotoxicity from cetyltrimethylammonium bromide (CTAB) surface layers and their challenging surface conjugation, due to ligand-exchange requirements.[21,22,24−27] While there has been a push to create non-CTAB conjugated, easily conjugatable Au monomers, such as nanopopcorn, at the present moment spectral tunability is more limited.[23] As an alternative, Au monomers can be assembled into chain-like structures ("nanochains"). Such fabricated Au nanochains can tune the plasmonic response,[28,29] because short interparticle distances ensure a strong plasmonic coupling along the chain (defined as the longitudinal surface plasmon resonance), and the most intense, and red-shifted, longitudinal surface plasmonic resonance is described as the super-radiant mode.[30,31] To quantify the tunability of nanochain systems, the D/r ratio is used as a measure of the gap distance (scaling with monomer size), defined as the center-to-center distance between the NP monomers in the chain and the radius of the NP monomer, respectively.[31,32] As shown by Willingham et al., D/r ratios below 2.4 are required so as to observe substantial plasmonic shifts, with smaller D/r ratios more desirable for increased tunability.[30] The narrow gap distances are also a great advantage of the nanochains, in contrast to nanoconstructs such as elongated nanorods, because intense photoinduced electric field hotspots are generated in the gaps of the chains, which have been shown to exhibit great intensity (higher than the corresponding elongated nanorod systems).[33,34] The well-documented electric field hotspots of nanochain systems[32,35,36] are highly advantageous; they have applications for surface enhanced Raman (SERS), super resolution, and single molecule microscopies, in addition to therapeutic utility (enhancement of photothermal therapy).[37−41] To fabricate narrow-gap nanochain systems, several methods have been developed, including template-based methods and template-free methods (interparticle force assembly).[42,43]

We report on a template-free, green, and scalable method for producing biocompatible gold nanobead chains. These nanobead chains are assembled through an electrostatic interaction, utilizing virgin surface Au NP monomer nanospheres with a diameter of 20 nm, produced by the pulsed laser ablation (PLA) method (Figure 1.1).[3,44] The PLA method has been chosen because it is a completely green synthesis that

https://doi.org/10.1021/acs.chemmater.1c00336
Chem. Mater. 2021, 33, 2913−2928

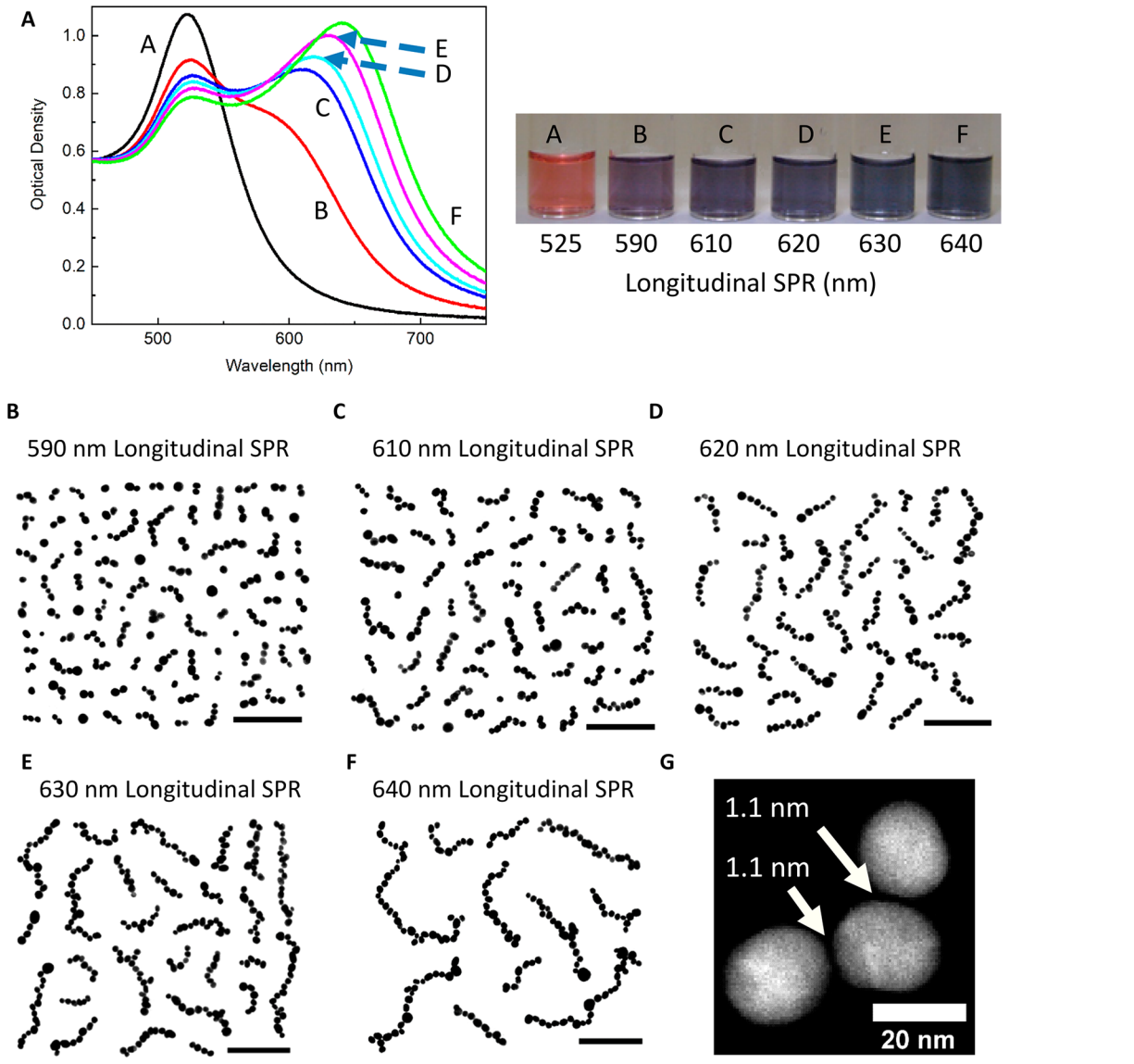

Figure 2. (A) UV−vis spectra of Au nanochains and color images for each of 6 samples, starting with the original monomer sample (525 nm peak) and continuing with samples of increasingly longer nanochain formation, which correlates with increasingly red-shifted super-radiant modes ranging from 590 to 640 nm. (B−F) Compositive TEM images of gold nanochains with longitudinal SPR ranging, respectively, from 590 to 640 nm (scale bar is 200 nm). (G) High-resolution TEM image of a gold nanochain trimer, revealing its narrow gaps.

produces, directly in deionized (DI) water, nontoxic, stable, and highly pure Au NP monomers, in contrast to chemical methods that involve chemical precursors and reducing agents, as well as stabilizing/capping ligands, such as citrate, so as to maintain colloidal stability.[45,46] As a metric for greenness, the atom economy of the PLA technique, defined as the ratio of the molecular weight of the product (Au colloid) compared to the molecular weight of all substances formed,[47] is nearly 100%.[45,46] Due to the PLA method, it is important to note that the generated Au NPs are partially oxidized by the oxygen present in the solution.[3,44] These Au−O compounds are hydroxylated, followed by a proton loss, giving the surface a natural negative charge, due to these $Au-O^-$ surface moieties; they can thus be readily surface conjugated.[48,49] In our previous studies we have demonstrated that the bare (virgin) PLA-produced Au surface does ensure a facile, rapid (1−2 h) and highly controllable conjugation of ligands, such as thiol terminated methoxy poly(ethylene glycol) (mPEG-SH), with a tunable surface coverage between 0 to 100%.[49,50] Also, efficient peptide and small molecule conjugation has been demonstrated on such PLA-produced Au monomers, with high molar ratios (on the scale of thousands of peptide groups per gold NP).[51,52] This unique feature of versatile and controllable surface manipulation and modification of the PLA-generated Au NPs, serves as the foundation in the present study for their assembly into Au nanochains with tunable longitudinal SPR, thus differentiating our method from former methods of template-free (electrostatic) nanochain assembly. By modifying the Au NP monomer surface with two different ligands, CALNN pentapeptide and cysteamine, a new type of highly linear, narrow gap nanobead chains was produced (Figure 1.2). The CALNN peptides were attached onto the NP surface via a cysteine attachment, because they are well-known ligands for improving NP colloidal stability while also hindering chain assembly.[53] In contrast, the cysteamine molecules were coated onto the nanoparticles via sulfhydryl (−SH) attachment,

https://doi.org/10.1021/acs.chemmater.1c00336
Chem. Mater. 2021, 33, 2913−2928

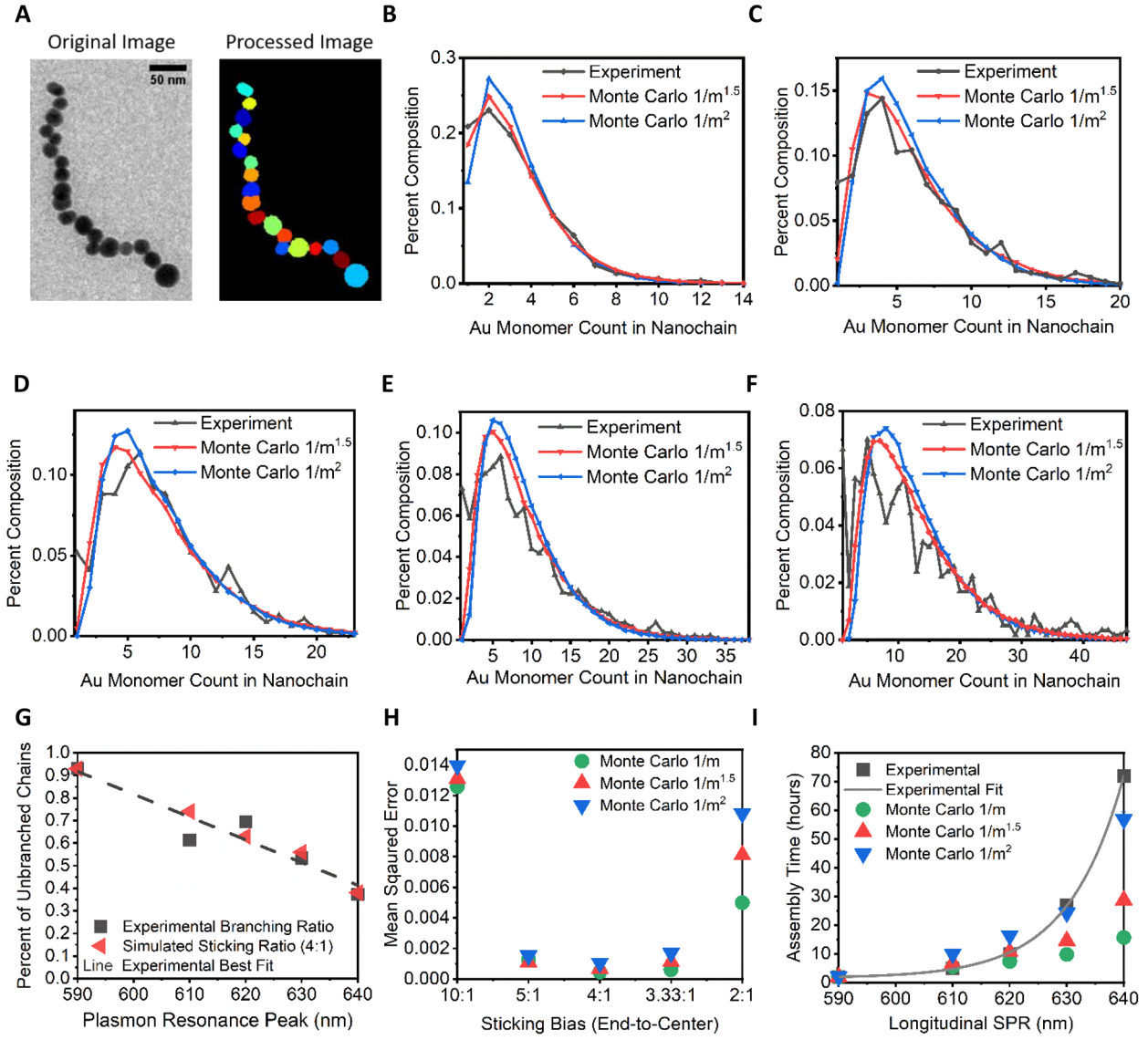

Figure 3. (A) Example nanobead chain processed through CellProfiler, in which 19 monomers are identified from the original image, each outlined by a solid color in the processed image. (B–F) Experimental and Monte Carlo ($d = 1/m^{1.5}$, $1/m^2$) monomer count distributions present in the 590 nm–640 nm longitudinal SPR samples. (G) Experimental and Monte Carlo (4:1 sticking bias) chain branching for each longitudinal SPR sample. The experimental sample is fitted (blue dashed line) with an $R^2 = 0.89$, showing close overlap with the 4:1 simulated sticking bias. (H) Mean squared error for various Monte Carlo simulated sticking bias, under varied rates of diffusion dependence ($1/m$, $1/m^{1.5}$, $1/m^2$); under all these conditions a 4:1 sticking bias exhibits the minimum mean squared error (MSE), when compared to experiment. (I) Experimental assembly time (gray) compared with Monte Carlo assembly time, under $1/m$, $1/m^{1.5}$, and $1/m^2$ dependent diffusion.

because their amine (−NH2) terminals are well-known to induce chain assembly via electrostatic attraction.[54,55] Utilizing the combination of both CALNN and cysteamine, nanochains can be formed over 24–72 h, with the period depending on the desired longitudinal SPR shift (Figure 1.3). Lastly, using UV–vis spectroscopy to "monitor" the chain assembly, the growth of the nanochains can be controllably quenched, at a given time, by adding thiol terminated methoxy poly(ethylene glycol) (mPEG-SH), as shown in Figure 1.4.

As demonstrated within the manuscript, the synthesized Au nanobead chains have short interparticle gap distances, indicating that they have a high D/r ratio (center-to-center distance between the NP monomers in the chain/radius of the NP monomer),[31] of great importance for optical and electric field hotspot enhancement.[30,35,36] The nanochains are assembled in an aqueous solution, with no solvent transfer required, and have high linearity (high morphological control) with easy-to-conjugate surfaces. Furthermore, the nanobead chains exhibit red-shifted tunable plasmon resonance, as well as an intense optical scattering. Due to the wide range of desirable properties that the nanobead chains possess, the nanobead chains should have great potential for *in vitro* and *in vivo* contrast imaging (optical scattering, SERS, photoacoustic, CT) and targeted theranostics, combining diagnostics and therapy.

2. RESULTS AND DISCUSSION

2.1. Synthesis and Physical Characterization of Au Nanobead Chains. Starting from 20 nm Au NP monomers having bare (virgin) surfaces, gold nanobead chains were synthesized as described in the Experimental Section. These gold nanochains display characteristic shifts in their UV–vis absorption spectra, with a new secondary peak first emerging at

https://doi.org/10.1021/acs.chemmater.1c00336
Chem. Mater. 2021, 33, 2913–2928

approximately 590 nm, which can be tuned to 640+ nm, in addition to the fixed primary "monomer" 525 nm peak (Figure 2A; Supporting Information Figure S1). The red-shifting of the UV−vis spectra is caused by the nanobead chains' growth, which occurs over a period of up to 72 h. The nanobead chain solution exhibits changes in color with time, with images taken after quenching at 2 (B), 5 (C), 10 (D), 27 (E), and 72 (F) h after chain assembly initialization. The long time scale for assembly is significant because longer time scales have been reported to be required to produce highly linear chains.[56] Yang et al. demonstrated that, when polymer-assisted nanochain assembly occurred over long time scales (8 h), samples were highly linear and the spectral band (longitudinal SPR shift) was sharp and pronounced.[56] For the nanochain assembly (up to 640 nm longitudinal SPR), the synthesized batch volume is 1 L (OD 1).

To better characterize the Au nanochains, samples with the longitudinal SPR at 590, 610, 620, 630, and 640 nm (super-radiant mode), respectively, were deposited on TEM grids for size analysis. Due to the low sample grid density, a combined image of TEM crops (single nanochains were aggregated into a single image) is given for every sample in Figure 2B−F. As the longitudinal SPR of the nanochains shifts toward the red end of the spectrum, longer chains do form.

Using high resolution transmission electron microscopy, the gap distance between the monomers was determined to be 1.1 nm ± 0.1 nm (example shown in Figure 2G; additional images in Supporting Information S2). Based on this gap distance and assuming a 20 nm Au monomer diameter, the D/r ratio (center-to-center distance between the NP monomers in the chain/radius of the NP monomer) of the synthesized nanochains is 2.11 ± 0.01, which lies in the region of strong plasmonic tunability.[32,57]

The stability of the Au nanochains (their shelf life) was tested by comparing the UV−vis spectra taken immediately after the 640 nm longitudinal SPR synthesis to the UV−vis spectra taken at 1, 2, and 4 months after synthesis, under room temperature storage conditions. As Supporting Information Figure S3 shows, no significant change in the UV−vis spectra occurs, revealing that the sample exhibits good long-term stability. Furthermore, intraparticle variability (batch-to-batch) was controlled using the UV−vis spectrum as a guide. As Supporting Information Figure S4 shows, the UV−vis spectrum matching of longitudinal SPR allows nanobead chains having comparable morphologies and lengths to be made (i.e., allows for reproducible fabrication of Au nanobead chains).

2.2. Nanobead Chain Ensemble Distribution, Linearity, and Assembly Kinetics. Transmission electron microscopy of the nanobead chains reveals that each sample is comprised of an ensemble of chain lengths. To quantify the nanochain ensemble, TEM images were acquired in batch for each sample and analyzed using CellProfiler, a machine vision (MV) software, so as to determine their monomer count distributions, with an example provided in Figure 3A and expanded description of CellProfiler given in the Supporting Information Figures S5 and S6.

As the nanobead chain distributions reveal (Figure 3B−F), the 590 nm longitudinal SPR sample is comprised of short chains with a narrow distribution (mean 3.3 ± 2.1 monomers), whereas the red-shifted longitudinal SPR samples have longer average lengths and wider distributions (6.1 ± 4.3; 7.4 ± 4.4; 8.9 ± 7.2; and 12.7 ± 10.2 monomers, respectively). In addition to the distribution of the monomer counts, the linearities of the nanobead chains, i.e., their ratios of unbranched chains, were determined for each sample utilizing the TEM images (Figure 3G). The linearity of the nanochains is a highly important feature of their plasmonic utility, as linear chains produce narrow, red-shifted plasmonic resonances, whereas globular (nonlinear, highly branched) chains produce broad and less red-shifted plasmonic resonances.[56] Furthermore, alongside the red-shifted plasmonic extinction, the electric field hot spots have been demonstrated to red-shift with the linear chain length, with the induced electric field magnitudes being the highest for linear chains (as opposed to when stacking occurs).[36] As shown in Figure 3G, the 590 nm longitudinal SPR sample has few branches, with greater than 90% of the samples still being unbranched (linear). By 630 nm longitudinal SPR, unbranched chains constitute approximately 50% of the total sample, and 50% of the chains do have branches. While longer longitudinal SPR samples do include branched chains, most of these branches are only 1−2 monomers long (Figure 2E,F); thus, the chains maintain an overall near-linear morphology.

The highly linear nature of the Au nanobead chains and the narrow interbead gaps is likely due to sample-dependent dipole−dipole interactions, where the dipole moments form at the ends of the nanochain during assembly and drive a preferential sticking of the nanometal beads.[58−60] To better quantify the chain-end-based sticking bias, Monte Carlo simulations were performed, using the experimental TEM mass distributions as a guide, under various end-to-center bead sticking biases (Supporting Information Figure S7; Figure 3H). Overall, a 4-to-1 end-to-center sticking bias best fits the experimental branching data (Figure 3G,H). This biased sticking probability during the nanochain assembly (4 times higher among end beads) accounts for the formation of these gold nanobead chains rather than the production of nanobead globules. We note that this 4:1 bias is in addition to the geometrical 5:4 bias introduced by the cubic lattice underlying the Monte Carlo simulation.

In addition to determining an optimal end-to-center sticking ratio for the nanobead chain assembly, we used the Monte Carlo simulations to determine the diffusion coefficient mass dependence of the assembly kinetics (Figure 3I). For nanoparticle self-assembly, the diffusion coefficient has been established as the driving parameter for the assembly kinetics.[61] By comparing the experimental assembly time to the Monte Carlo assembly times, we find that the chain assembly kinetics best fit at a $1/m^2$ dependent diffusion coefficient (across inverse power intervals of 0.5). Interestingly, for the 590−610 longitudinal SPR samples, a $1/m^{1.5}$ diffusion coefficient dependence best fits the experimental assembly time (MSE = 2.43, 1.17, 21.4 for $1/m$, $1/m^{1.5}$, $1/m^2$). However, over all the samples, the $1/m^2$ diffusion coefficient dependence has the smallest mean squared error (>6.7×) when compared to experiment (MSE = 696, 406, and 60.4 for $1/m$, $1/m^{1.5}$, and $1/m^2$). We hypothesize that the diffusion coefficient's inverse mass power dependence may increase as the chains grow, in part due to the increasing fractal dimension of the chains, thus lengthening the assembly time.[61] To better demonstrate the extended assembly time under the higher inverse mass diffusion coefficients for longer SPR tuning, time-resolved Monte Carlo movies are provided as described in the Supporting Information Figure S8 for $1/m^{1.5}$- and $1/m^2$-like assembly at 640 nm longitudinal SPR. Furthermore, we have

https://doi.org/10.1021/acs.chemmater.1c00336
Chem. Mater. 2021, 33, 2913−2928

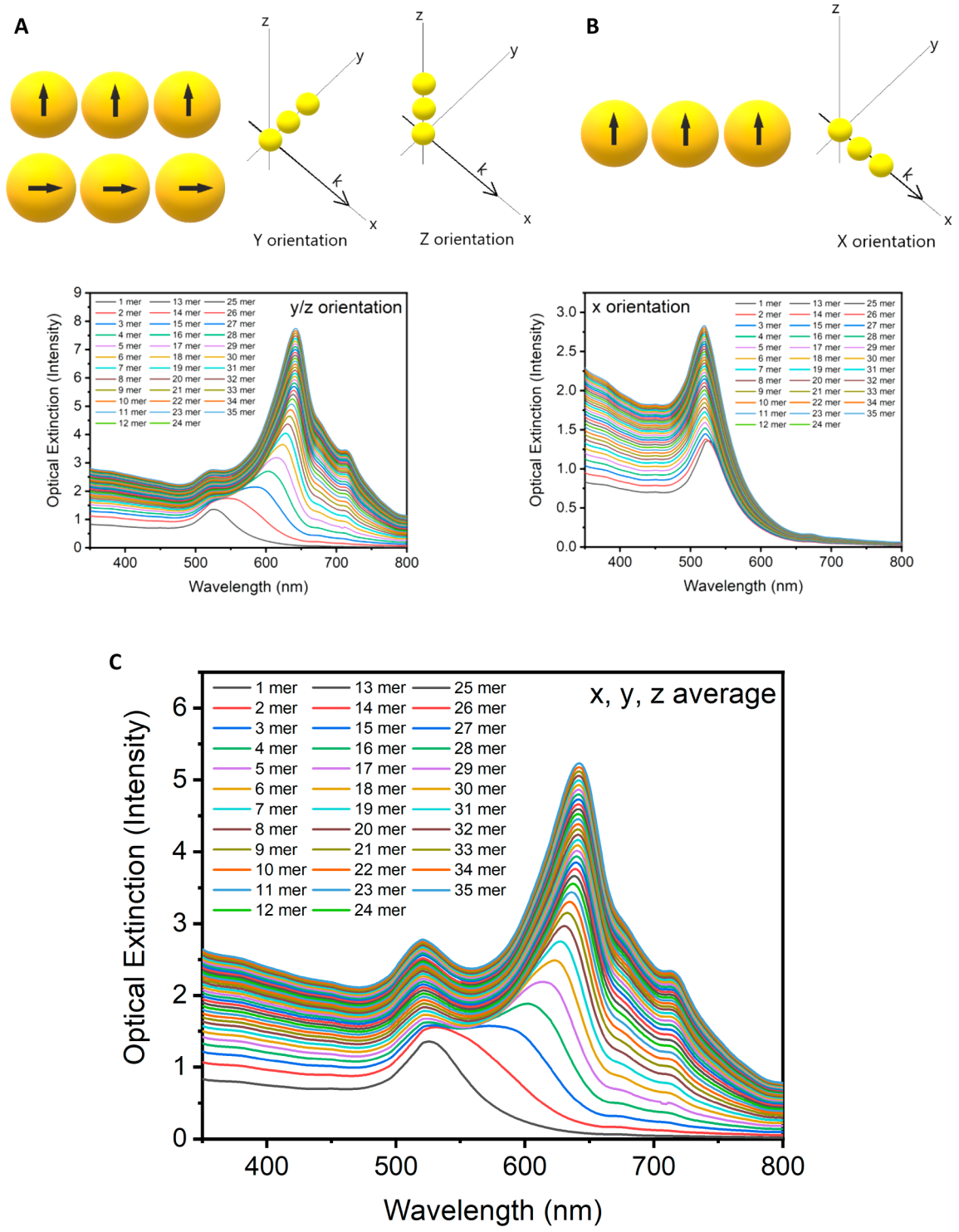

Figure 4. Optical extinction spectra computed for linear chains (up to 35-mer), assuming a 1.15 nm gap between monomers. (A) Linear extinction spectra along the *y* and *z* orientations. Both electric field orientations of the incoming light (*k* vector) are averaged, so as to simulate excitation from unpolarized light, with the *y* orientation e-field vectors shown above. (B) Linear extinction spectra along the *x* orientation. Due to the electric field symmetry, both electric field orientations lie transverse to the chain; thus, the longitudinal SPR shift is not observed. (C) Total spectra for 1.15 nm monomer-to-monomer gap containing linear chains, from averaged *x*, *y*, and *z* orientations (equal weight along each orientation) for each chain length.

reported the chain monomer distributions for both 1.5 and 2.0 inverse power dependent diffusion coefficient samples, utilizing a 4-to-1 end-to-center sticking bias ratio, which shows close agreement to experiment (Figure 3B–F). It is also worth noting that, regardless of the diffusion coefficient mass dependence used ($1/m$, $1/m^{1.5}$, $1/m^2$), the 4-to-1 end-to-center bead sticking ratio produced the smallest mean squared error (Figure 3H).

Overall, the Monte Carlo simulations provide an important insight into the chemical nature of the synthetic method used,

https://doi.org/10.1021/acs.chemmater.1c00336
Chem. Mater. 2021, 33, 2913–2928

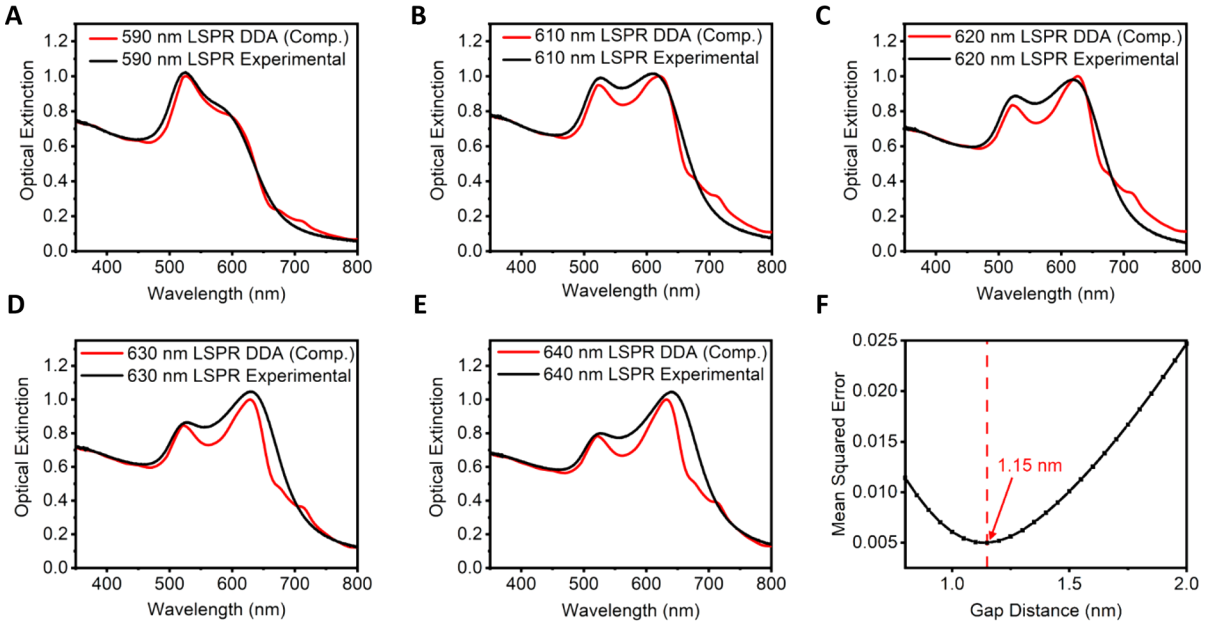

Figure 5. (A–E) Computationally generated (red curve) and experimental (black curve) optical extinction spectra for samples with longitudinal SPR ranging from 590 to 640 nm; the DDA computations utilized chain length distributions determined by TEM and a gap distance of 1.15 nm. (F) The mean squared error (MSE) between simulated and experimental spectra as a function of the gap distance. A gap distance of 1.15 nm is found to have the smallest mean squared error.

where attachment to bead-chain "end units" is favored over attachment to bead-chain "center units". Furthermore, the nanobead chain assembly is shown to be driven by a higher-than-expected inverse mass order dependent diffusion of the Au bead monomers. For most self-assembled systems, the diffusion kinetics is frequently assumed to be $1/m$ or $1/m^{\text{fractal dimension}}$ (for such systems the fractal dimension is typically < 1.5).[61] However, as our Monte Carlo simulations reveal, higher inverse order bead nanochain diffusion dependence (d = 2.0) best correlates the Monte Carlo simulation kinetics to the experimental assembly kinetics. This unexpected trend has been reported by other groups for liquid-based nanochain assembly, and several hypotheses on the high inverse order diffusion coefficient dependence have been proposed, including viscosity (drag, liquid layering) and surface interactions among the nanoparticles.[61−64]

2.3. Simulation of the Optical Extinction Spectra and Gap Distance of the Gold Nanobead Chains. In the field of plasmonics, while it is known that plasmonic computations can highly predict the optical properties, such as the extinction spectra of NP monomers, a significant challenge has been to quantitatively relate experimental optical spectra to computational optical spectra for complex nanosystems.[65,66] For complex layered systems, such as Au NP thin films, close correlation has been demonstrated between experimental and computed plasmonic properties,[66] however for colloidal Au systems such as nanochains, the chain length distribution produces several challenges for computing the spectra.[65] Indeed, establishing quantitatively a clear correlation between TEM and UV–vis extinction data faces large challenges: (1) Chains should have few branches, and disordered aggregation should be avoided when depositing the samples onto the TEM grids.[65] (2) A quantitative correlation relating TEM distributions to UV–vis spectra requires all the UV–vis contributing elements from within the TEM distribution (monomer, dimer, trimer, etc.) to be known. Because the nanobead chains synthesized in this work are highly linear, the first issue of quantitative correlation can be overcome by depositing samples onto TEM grids with low density. To help with the second issue, we have used the discrete dipole scattering (DDSCAT) package to compute the optical spectra of all the linear chains within the TEM distribution, as shown in Figure 4. Performing such DDSCAT computations is typically not feasible for long chain lengths (10+ monomers), as prior to this publication DDSCAT had not been parallelized to allow computations to be performed on multiple cores. To overcome this computation bottleneck, we developed a Python script to run the DDSCAT on a Linux-based SLURM cluster, running such computations on up to 400 parallelized cores, where parallelization was split along the excitation wavelength (350–800 nm). Hence, instead of a single core computing all the optical wavelength samples so as to determine the optical extinction, each core only computed 1–2 wavelength samples, thus accelerating the computation time by approximately 2 orders of magnitude.

Utilizing a linear combination of chains and their frequencies from the TEM distributions, spectra were weighted and a combined spectrum was generated (Figure 5A–E). Within each spectrum we can see both a transverse SPR mode (near 520 nm) and a longitudinal SPR mode (590+ nm). Overall, both the DDA transverse SPR and the longitudinal SPR mode closely match the experimental results.

The gap distance (distance between monomers) is an important parameter that determines the spectral properties of the nanochains. Due to the gap distances being less than 2 nm, determining accurate distances experimentally is challenging, expensive, and time-consuming, as high resolution TEM must be used. Hence, for the simulations performed, we tested whether we could predict the gap distance via DDA. To do so, the mean squared error value (eq 2 in the Experimental Section) was determined for each spacing between 0.75 to 4.00 nm, so as to determine the best fit. Overall, a 1.15 nm gap

https://doi.org/10.1021/acs.chemmater.1c00336
Chem. Mater. 2021, 33, 2913−2928

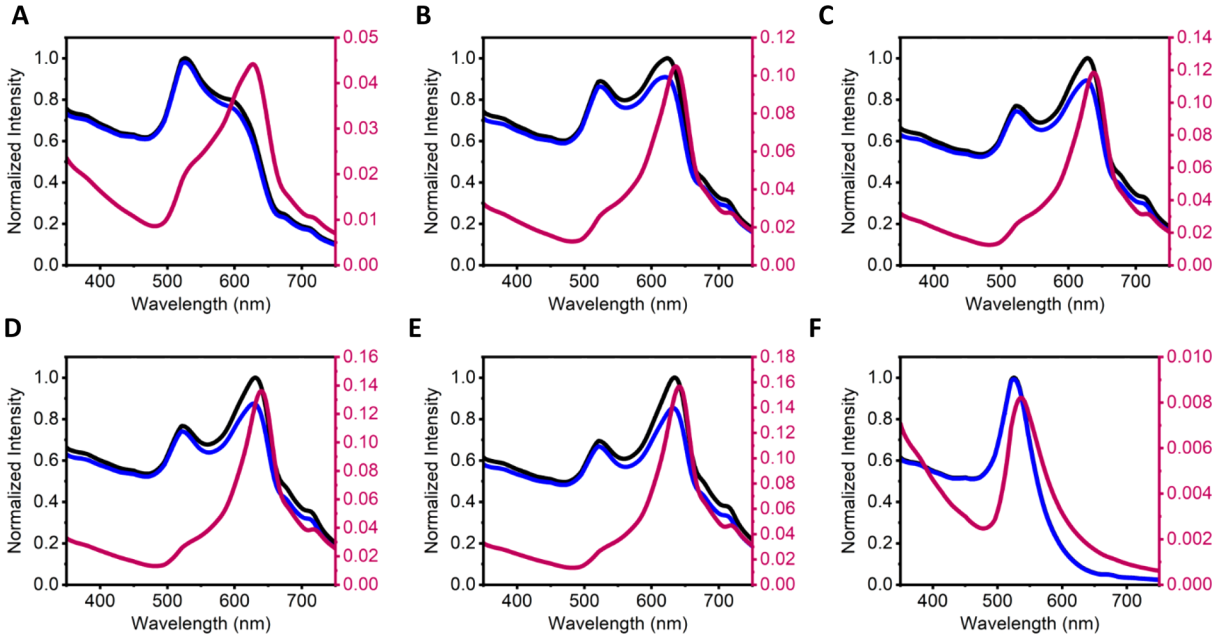

Figure 6. Relative components of absorption (blue; left axis) and scattering (purple; right axis) that compose the optical extinction spectra (black; left axis) for each sample. A, 590 nm; B, 610 nm; C, 620 nm; D, 630 nm; and E, 640 nm longitudinal SPR; and F, 525 nm (monomer) plasmon resonance maxima, all determined via DDSCAT simulation using a 1.15 nm gap distance. As the chain length grows, the scattering contribution to the extinction coefficient grows rapidly: A shift from a 0.8% contribution (monomer) to a 16% contribution occurs at 640 nm longitudinal SPR. In terms of maximum scattering intensity compared to the maximum monomer scattering intensity, the scattering amplitiude increases by 6.92×, 20.2×, 24.77×, 29.27×, and 39.45×, respectively, for the 590, 610, 620, 630, and 640 nm longitudinal SPR. Note that, for the monomer sample (F), the black line (extinction) is hidden behind the blue line (absorption) due to their close overlap.

distance gave the best average fit, among all the samples (Figure 5F). The DDA predicted value of a 1.15 nm gap distance is in excellent agreement with the experimentally measured average gap of 1.1 nm ± 0.1 nm. Furthermore, it should be noted that, based on the gap distance deviation measured from experiment (±0.1 nm) and the very similar MSE from 1.0 to 1.30 nm, the gap inhomogeneity only has a minor effect on the spectral shifts; hence, the 1.15 nm gap distance is a good approximation of the nanochain ensemble.

Overall, based on the DDA simulation results, we observe that, as the chains grow longer, length-dependent tunable red-shifting is predicted, in close correlation with experiment. Furthermore, the DDA simulation correctly predicts the experimentally observed average gap distance between the chains. These results allow for a "simulated dissection" of the nanochain ensemble to the level of a single nanochain, and in the following section, optical scattering properties of immense biophysical utility are further explored using the DDSCAT method, coupled to the experiment.

2.4. DDA-Computed Gold Nanochain Optical Scattering, Dark-Field Light Scattering Microscopy, and MTT Cytotoxicity Assay. In addition to determining the optical extinction spectra for each nanobead chain sample, the absorption and scattering contributions to the extinction coefficient were also calculated in DDSCAT, using a 1.15 nm gap distance, as shown in Figure 6. The scattering component of the nanochains is particularly of high biophysical importance, as gold nanoparticles are frequently used for optical scattering applications. In our simulations we see the following: As the length of a linear cluster of Au NPs grows longer, the scattering contribution to the extinction coefficient substantially grows (from a 0.8% contribution in the monomer to a 16% contribution in the 640 nm longitudinal SPR sample). This increased scattering cross-section, of approximately 40× enhancement in the scattering amplitude, is a major advantage of using gold nanochains as probes in optical scattering-based imaging, like dark-field optical microscopy.

To demonstrate the biophotonic application of the DDA-predicted intensely optically scattering nanobead chains, with an active targeting enhancement, RGD peptide-conjugated gold nanobead chains, with a longitudinal SPR at 640 nm, were incubated with HeLa cancer cells and then imaged under dark-field optical microscopy (Figure 7B). The gold nanobead chains with longitudinal SPR at 640 nm were selected for the dark-field optical imaging because they have the reddest excitation wavelength (with deeper tissue penetration depths) and highest maximum scattering cross-section among all samples (strongest scattering signal). In contrast, RGD peptide-conjugated Au NP monomers (surface plasmon resonance at about 525 nm) were also incubated with HeLa cancer cells, as a control for comparing image properties (Figure 7A). Nontargeted controls (Au monomers and 640 nm longitudinal SPR chains with no attached RGD peptide) were also incubated in HeLa cells to demonstrate the potential for nanochain-assisted active targeting. As shown in Figure 7A,B, the HeLa cancer cells stained with Au NP monomers and gold nanobead chains appear green and orange, respectively, under dark-field optical microscopy. This is because the surface plasmon resonance of the gold nanostructures determines the image color when they are used as contrast agents in dark-field light scattering imaging. For the Au NP monomer nontargeting ligand control (Figure S9 in the Supporting Information), speckled regions are practically nonexistent due to the low uptake efficiency of the Au NPs. This result is consistent with our previously published results, showing a large enhancement due to RGD-driven active targeting in the HeLa cells (10% *in*

https://doi.org/10.1021/acs.chemmater.1c00336
Chem. Mater. 2021, 33, 2913−2928

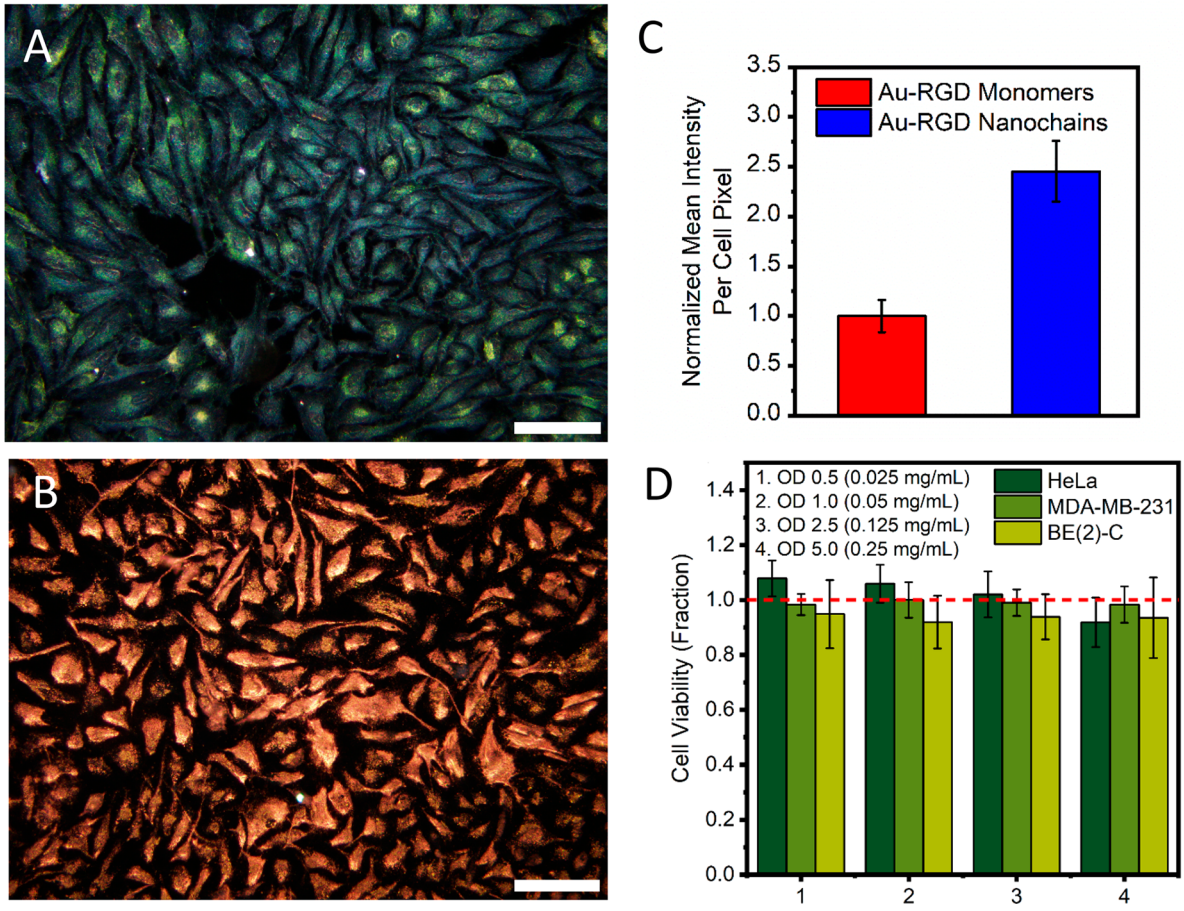

Figure 7. Dark-field light scattering images of human HeLa cancer cells stained with (A) 20 nm RGD peptide-conjugated Au NP monomers and (B) RGD peptide-conjugated Au nanochains with longitudinal SPR at 640 nm. The scale bar is 100 μm. (C) Mean intensity per cell pixel (n = 12 cells) for HeLa cells incubated with 20 nm RGD-conjugated Au monomers and RGD-conjugated 640 nm longitudinal SPR nanochains (equal incubation masses). (D) MTT assay under gold nanobead chain (longitudinal SPR at 640 nm) incubation for HeLa (cervical cancer), MDA-MB-231 (breast cancer), and BE(2)-C (neuroblastoma) cells, for ODs between 0.5 and 5.0 (0.025 mg/mL−0.25 mg/mL NP mass concentration), revealing that the gold nanochains are biocompatible, i.e., show no statistically significant cell toxicity effects.

vitro uptake for RGD-driven active uptake compared to <2% for nonactive uptake).[50] For the Au nanochain (with longitudinal SPR at 640 nm), very few speckled regions appear for nontargeting ligand control, although there were more speckled regions compared to that observed for Au NP monomer nontargeting ligand control (Figure S9 in the Supporting Information). These results demonstrate the great potential of the Au nanochain for use as an active targeting platform, because various moieties can be conjugated to the surface of the nanochain so as to promote cellular uptake.

To quantify the dark field scattering enhancement for the nanochains, the scattering intensity for individual cells within each image (Figures 7A,B) was measured. The RGD-conjugated Au monomer incubated cells have a mean intensity per pixel of 48.0 ± 7.8 and the RGD-conjugated Au nanochain incubated cells have a mean intensity per pixel of 118.0 ± 14.5 (Figure 7C), revealing that the Au nanochains have a 2.46× ± 0.50× greater mean scattering intensity per Au nanosphere, compared to the Au monomer nanospheres. The scattering increase of the Au nanobead chains, by a factor of 2.46 ± 0.50, reveals the benefits of the Au nanochains for dark field imaging, as equal masses of gold (equivalent masses of gold nanospheres) were added for both the Au nanobead chain and the Au monomer samples during cell incubation. This enhancement by about 2.5 also closely resembles the DDA predicted per nanosphere enhancement value of 3.35 ± 0.55 (Supporting Figure S10) and may be a bit smaller due to a somewhat less efficient uptake of the larger Au NPs by the HeLa cells. Note that Albanese et al. show that Au NPs on the scale of 20 nm have 20−30% better cell uptake than larger Au aggregates of similar dimensions of the nanochains (100−200+ nm in length).[67] In addition, we can tell from Figure 7A,B that the distribution of the internalized Au nanochains is similar to that of Au monomers, since Figure 7A,B shows that the internalized Au nanoparticles were spread out in a uniform manner within the entire cell for both Au monomers (Figure 7A) and Au nanochains (Figure 7B).

Applying the gold nanobead chains as imaging contrast agents presents multiple advantages. Foremost, because the longitudinal SPR of the gold nanobead chains is tunable, optical imaging at a selected wavelength, avoiding background from cell scattering or other scattering/fluorescent dyes, is possible. Second, images with high brightness could be acquired using the gold nanobead chains, because of the highly enhanced scattering cross section relative to that of the NP monomer. Third, it is advantageous to tune the gold nanobead chain optical properties (absorption, scattering) to redder wavelengths for studying thick cell layers (>1 μm) or for performing *in vivo* imaging, because red light travels deeper into tissue, by a factor of 10−100×, compared to bluer light,

https://doi.org/10.1021/acs.chemmater.1c00336
Chem. Mater. 2021, 33, 2913−2928

with much lower background fluorescence. Fourth, the gold nanobead chains synthesized here can be easily conjugated with active targeting moieties, like the RGD peptide shown in Figure 7, for *in vitro* and, most importantly, for *in vivo* targeting. Fifth, the gold nanochains have intense electric field hotspots between monomers,[32,35,36] further enhanced by their linearity, as demonstrated previously by Pazos-Pérez et al.[36] These electric field hotspots would serve as an advantage in surface-enhanced Raman spectroscopy (SERS) microscopy to drive sensitive detection and imaging of biomaterials, for example, imaging in cancer tissue.[32,40,68] Hotspots in nanochains could also enhance near-field coupling with fluorescent dyes, currently of immense interest in super resolution and single molecule imaging.[37−39] It should also be noted that these intense e-fields have therapeutic relevance, as it was demonstrated that they significantly reduced the laser fluence threshold needed to achieve optical breakdown during photothermal therapies.[41]

Lastly, of immense clinical importance, the nanochain biocompatibility (640 nm longitudinal SPR) was tested across three different cancer cell types (breast cancer, cervical cancer, brain cancer), up to a mass concentration as high as 0.25 mg/mL, via MTT assay (Figure 7D). Overall, no statistically significant cell toxicity from the gold nanochains was observed (Figure 7D). This results in, no significant toxicity effects, across a variety of cell lines, showing the nanochain system to be well-suited for a variety of biomedical applications. In addition to serving as optical and CT imaging nanoagents, cancer cell targeted gold nanochains could potentially also serve as targeted nanocarriers of photosensitizers for photodynamic therapy and photothermal therapy, ligand-activated chemotherapy, and radiotherapy.[14,15,69−71]

3. CONCLUSION

Overall, we have reported on the green synthesis of highly linear, narrow-gap, gold nanobead chains, exhibiting spectral tunability into the far-red and intense optical scattering. On the theoretical front, by combining an experimental approach with Monte Carlo and DDA simulations, we are better able to understand the assembly kinetics and optical properties of the nanochains, from and at the level of a single monomer, thus, better enabling rational design of such nanobead chains for biophotonic applications. For example, utilizing ensemble statistics of the nanobead chains, determined by a TEM image analysis, we observe that elongated, highly linear chains do form, with the Monte Carlo assembly simulations providing an interesting insight into the underlying selectivity of the specialized chemical synthesis, where the bead chain-end units of these linear clusters of Au NPs are about 4 times more reactive than their bead chain-center units; thus, linear gold nanobead chains, rather than globular assemblies, are formed. It is this linear chain assembly that enables the spectral tunability property of the gold nanochains, and this tunability is of high potential value for the biophotonic applications of the nanochains. Furthermore, the DDA method, in tandem with *in vitro* experiments, demonstrates the elongated chain-based (640 nm longitudinal SPR) optical scattering enhancement, relative to nanosphere monomers. Lastly, we demonstrated that these nanobead chains are highly biocompatible, easy to conjugate, and advantageous for scattering-based applications, thus having great potential utility for a wide range of biomedical applications, such as enhanced *in vitro* and *in vivo* contrast imaging (optical, photoacoustic, and CT), diagnostics, and targeted theranostics. It should be noted that we have demonstrated that *in vivo* the nanochains disassemble within 1−4 weeks, this biodegradability adding to their medical utility, as *in vivo* clearance is improved.[19] Future research on these Au nanochain systems may proceed along three directions: (1) Batch synthesizing and characterizing longer nanochains, with a goal to achieve NIR longitudinal SPR (small scale assembly of up to NIR 710 nm longitudinal SPR nanochains was achieved, as shown in the Supporting Information S1, with subsequent optimization planned); (2) exploring how the molar ratio between the CALNN peptides and the cysteamine molecules attached onto the surfaces of the Au NPs affects the growth of these Au nanochains, their gap distance (smaller gaps are more desirable as they will result in redder spectral shifts), and the chain branching (its reduction will help moving the SPR to the infrared); and (3) utilizing these nanobead chains for additional *in vitro* and *in vivo* studies. Our results demonstrate that these biocompatible Au nanobead chain systems exhibit many novel properties, including spectral tunability and intense optical scattering cross sections; we thus expect them to be utilizable for a variety of photonic and biomedical applications, such as scattering-based dark-field, photoacoustic, and X-ray imaging, as well as targeted nanotheranostic modalities.

4. EXPERIMENTAL SECTION

4.1. Materials and Instrumentation. All chemicals were used as received without further purification. mPEG-SH with a molar mass of 5000 g mol^{-1} (mPEG 5k-SH) was purchased from Creative PEGWorks (Chapel Hill, NC). Both cysteine-modified arginine−glycine−aspartic acid (RGD)-containing peptides with an amino acid sequence RGDRGDRGDRGDPGC and pentapeptide ligand with an amino acid sequence CALNN having purity higher than 95% were custom-synthesized by RS synthesis LLC (Louisville, KY). Cysteamine (CAS Number: 60-23-1) with purity higher than 95% was purchased from Sigma-Aldrich. PEG, peptides, and cysteamine were in powder form and dissolved in deionized water having an electric conductivity less than 0.7 $\mu S\ cm^{-1}$. All solutions were freshly made as needed and used within 12 hours. UV−vis absorption spectra were recorded by a spectrophotometer (UV-3600, Shimadzu Corp., Japan).

4.2. Production of the Colloidal Au NPs. We first produced primary spherical colloidal Au NPs having virgin surfaces, to be used for the fabrication of gold nanochains via a physical method of femtosecond PLA of a bulk Au target (Purity: 99.99%) immersed in DI water, as described in our previous publication.[49] This method uses tightly focused microjoule (μJ) femtosecond laser pulses to produce NPs, and the size/size distribution of the generated NPs can be precisely controlled by optimizing laser parameters, such as wavelength, pulse energy, duration, and repetition rate.[49]

Briefly, the ytterbium-doped femtosecond fiber laser (FCPA μJewel D-1000, IMRA America, Ann Arbor, MI), operating at 1.045 μm, delivered laser pulses at a repetition rate of 100 kHz, with 10 μJ pulse energy and 700 fs pulse duration. The emitted laser beam was first focused by an objective lens and then reflected by a scanning mirror to the surface of the bulk gold target, which was submerged in flowing deionized water (18 MΩ cm). The size of the laser spot on the gold target was estimated to be 50 μm, and its position was precisely controlled by the scanning mirror. Colloidal Au NPs with an average diameter of 20 nm were produced by this PLA method and used in our experiments. The generated nanoparticles have a narrow size distribution and have an absorption peak at 520 nm due to the localized surface plasmon resonance.[39] For Au NP monomers, 7 L of OD 1 solution can be made in 6 h.

It is worth mentioning that, during the PLA, the generated Au NPs are partially oxidized by oxygen present in the solution. These Au−O compounds were hydroxylated, followed by a proton loss, to give a surface of Au−O^-.[72] Therefore, the Au NPs produced using the PLA

https://doi.org/10.1021/acs.chemmater.1c00336
Chem. Mater. 2021, 33, 2913−2928

method are naturally negatively charged, and no capping agents or stabilizing ligands are required for maintaining their colloidal stability. This unique feature of having a virgin surface because of a capping agent-free procedure does allow versatile surface modifications for obtaining Au NPs with controllable surface chemistry,[49] which is utilized in the present study to assemble them into spectrally tunable gold nanochains.

4.3. Characterization of the Au Nanoparticle Surface Coverage. To characterize the surface coverage of Au nanoparticles, dynamic light scattering (DLS) was used to measure the increase in the Au NP radius after the small molecule (i.e., peptide) coverage. Dynamic light scattering has been used before to study surface conjugation of Au NPs by peptides.[73,74] In brief, the hydrodynamic diameter of the peptide-modified (CALNN peptide in this study) gold nanoparticle monomer nanospheres (20 nm), which includes the nanoparticle surface coating and the hydrated water ions, is measured (Malvern Nano Zetasizer ZS90 DLS). The Malvern Nano Zetasizer DLS is equipped with a 633 nm He−Ne laser, and an avalanche photodiode serves for detecting the scattered light at a 90° angle. In a standard measurement made in the automated mode, the instrument selected the attenuation factor and then recorded between 12 and 16 runs, measuring the dynamic light scattering (DLS) of the nanoparticles, which was determined by their Brownian motion, for calculating the intensity-average diameter. Three successive DLS measurements were performed for each sample, and the mean diameter increase was reported with the error bar corresponding to the standard deviation over these three measurements. As shown in Supporting Figure S11, a 20 000:1 molar peptide ratio is required for surface saturation, indicating that CALNN (2400:1; approximately 40−50% surface coated), cysteamine (1800:1), and mPEG-SH (200:1) molar ratios used in this study will not result in complete surface coverage for the 20 nm Au monomers.

4.4. Self-Assembly of Au NPs into Nanochains. In a typical process, colloidal Au NPs with an average diameter of 20 nm (STD 3 nm) and a zeta potential of −40 mV were mixed with a pH 7.0 aqueous solution of CALNN peptides, so as to achieve a defined molar ratio of 2400:1 between the CALNN peptides and the Au NPs. The mixture of Au NPs and CALNN peptides was kept undisturbed for 2 h at room temperature so as to enable sufficient conjugation of CALNN peptides to the Au NPs via gold−sulfur bonds. Following the surface conjugation of the CALNN peptide, the Au NPs were further modified with cysteamine molecules, by mixing with the cysteamine solution, so as to achieve a molar ratio of 1800:1 between the cysteamine molecules and the Au NPs. The solution was kept undisturbed until observing a significant color change, from red-pink to blue, which typically occurs between 24 to 72 h after the addition of cysteamine and serves as clear evidence for a successful self-assembly of NPs into nanochains.

Furthermore, gold nanochains with controllable lengths and tunable longitudinal SPR were fabricated by quenching the growth of the nanochains via binding mPEG 5k-SH molecules onto them after their longitudinal SPR reaches a desired wavelength. This was done by adding a solution of mPEG 5k-SH so as to achieve a molar ratio of 200:1 between the mPEG 5k-SH molecules and the Au NPs. The PEG molecules can stop the growth of the nanochains because they introduce steric repulsions between the Au NPs. Notably, PEG with molecular weight of 5000 Da specifically has been used by other groups (i.e., Scott et al.) in biological nanochains so as to reduce adsorption.[75] In the present study a total of five samples of gold nanochains were produced, with the longitudinal SPR ranging from 590 to 640 nm.

In our search of the CALNN and cysteamine ratios to be used for fabricating the gold nanochains, our principle for determining the appropriate ratio was to choose the minimal amounts of CALNN and cysteamine necessary for inducing the self-assembly of Au NP monomers into stable nanochains. By minimizing the molar ratio of each component, there remains enough empty space on the surface of the nanochains for subsequent conjugation of other functional ligands. Based on this principle, we found ratios of 2400:1 and 1800:1 to be the best ratios, respectively, for the CALNN/Au NP and cysteamine/Au NP conjugations. Furthermore, in terms of the pH stability, Jia et al. show that CALNN conjugated Au NPs have stable colloidal properties for pH < 10.[76] For cysteamine, within the range of pH 4−10, Au−cysteamine aggregates have been shown to be stable, with pH > 10 resulting in the deprotonation of the sulfur moiety, leading to destabilization of the product.[55,77] Notably, our *in vitro* experiments were performed at pH = 7.4, under stable pH conditions.

4.5. Transmission Electron Microscopy (TEM) and Image Analysis. Nanochain samples were deposited on TED Pella (trade name) 200 Cu mesh grids (Lot no. 160419). To determine the mass distributions of Au nanochains, TEM imaging was performed at 80 kV on a JEOL JEM 1400 transmission electron microscope. For every sample, 3 grids were analyzed with over 50 images taken per grid at 10 000× magnification. The interparticle variability of the nanochains was determined by taking over 150 TEM images for each sample across 3 grids. Namely, >50 images per grid were taken along all regions of the grid (edge, center) to ensure that 1.) Enough images were captured to accurately encapsulate the statistical ensemble of chain length distributions, 2.) By utilizing 3 grids and imaging across all grid locations, bias due to sample deposition was avoided. As such, for each sample, respectively, 1833 (590 nm), 607 (610 nm), 465 (620 nm), 1447 (630 nm), and 589 (640 nm), individual nanoparticles were analyzed so as to generate the experimental distributions.

After image acquisition, individual nanochains were cropped via ImageJ from the raw images. Following cropping, to identify the number of monomers in each nanoparticle, the images were analyzed using the CellProfiler program.[78] In brief, CellProfiler can identify objects using an intensity threshold (lowest accepted pixel intensity compared to max intensity) and the shape of the object (circular), and has been shown to be a useful tool to conduct quality control for properties like the size and shape of nanoparticles and nanoparticle aggregates.[79] For this study, thresholds of 60, 70, and 80% were tested for identifying individual monomer shapes. As the sample images show in Supporting Information Figure S5, the CellProfiler output identifies individual monomers from their circular outline (the monomers identified are given separate colors). After identification, the number of counted monomers within a nanochain is summed together to determine the total number of monomers per nanochain. Due to the intensity variation between samples, the highest count was selected among the 60, 70, and 80% thresholds (Supporting Figure S6).

High resolution TEM microscopy was utilized to determine the gap distance (spacing) between monomers in the Au nanochains. The high resolution microscopy was performed on a JEOL JEM 2100F scanning transmission electron microscope. Under such conditions, pixel resolution is 0.05 nm using the highest (2 500 000×) magnification. After acquiring high resolution TEM images, gap distances were analyzed using the ImageJ "measure" tool on raw (unadjusted) intensity data by importing image data with the NIH developed DM3 Reader Plugin (https://imagej.nih.gov/ij/plugins/DM3_Reader.html). Note that, to preserve image fidelity, DM3 images were utilized for gap distance determination instead of converting images to a compressed format. For each gap distance, measurements were collected three times and averaged to determine the error (standard deviation reported).

4.6. Monte Carlo (MC) Simulations. A number of NPs (monomers), equal to the total number of NPs for each experiment, is randomly placed on a cubic lattice with fixed concentration ($c = 10^{-3}$ for the three-dimensional lattice). It should be noted that cubic lattices have been shown congruent to "off-grid" MC simulations (clusters can assemble with infinitely fine grids); thus, we utilize the 6-sided cubic lattice.[80−83] The monomers are considered to be clusters of size $s = 1$. Diffusion of the clusters starts by randomly choosing a cluster and allowing it to move to a neighboring position, which consumes one microstep. The diffusion constant D is considered to be inversely proportional to a power d of m, the mass.[84−86] Thus, a random number $x \in (0, 1)$ is chosen, and if $x < 1/m^d$ the cluster diffuses by moving one cell length in a random direction to a neighboring site (or sites) on the lattice, assuming they are not

https://doi.org/10.1021/acs.chemmater.1c00336
Chem. Mater. 2021, 33, 2913−2928

already occupied by the NPs of another cluster (excluded volume condition). If two or more clusters contact each other (i.e., there are monomers at neighboring sites), they merge into one cluster with a (sticking) probability that depends on the position of the contacting NPs in the cluster. The ratio p of the sticking probabilities of end vs center particles was tested at 0.01, 0.1, 0.15, 0.2, 0.25, 0.3, 0.33, 0.5, and 1.0. Thus, we have $p = 1$ if the contacting monomers of both clusters are at the end of their cluster and $0.01 \leq p \leq 1.0$ otherwise. For each monomer we keep track of the number n of neighboring monomers to which it is connected. Thus, a lone monomer (cluster of size $s = 1$) has $n = 0$, the monomers of a cluster with size $s = 2$ both have $n = 1$, and a cluster with size $s = 3$ has two monomers (at the edges) with $n = 1$ and a central monomer with $n = 2$. A cluster's monomers that have $n = 0$ or $n = 1$ are considered to be at the end of the cluster. Other monomers in a cluster with $n > 1$ are "central". Sticking to them has the adjusted probability provided above (0.01−1.0).

The time after each step is increased by $\Delta t = 1/N$ (one MC microstep), where N is the number of clusters remaining, regardless of whether the cluster moved or not.[87−89] Clusters of increasing size s are formed as the simulation proceeds, and the simulation stops when the number N of the remaining clusters becomes equal to the number of clusters in the target experimental sample. Whenever two objects (particles or clusters) are merged into one, they are combined irreversibly, and the number of neighbors of the contacting monomers is increased by 1, with periodic boundary conditions utilized. Monte Carlo simulations are run 100 times per sample, and the cluster distributions are averaged.

4.7. Discrete Dipole Approximation (DDA) Calculations. Discrete dipole calculations were performed using DDSCAT ("Discrete Dipole Scattering") version 7.3.2 to compute the optical extinction coefficient, absorbance, and scattering spectra of linear clusters of Au NPs in an aqueous medium ($n = 1.33$). Reviews of the discrete dipole approximation technique and DDSCAT have been provided by previous authors.[90,91] To run DDSCAT, several user inputs are required: (1) the complex polarizability of Au, (2) the geometry of the Au NP clusters, and (3) the effective radius of the Au NP chains (see eq 1). The complex polarizability (function of wavelength from 300 to 800 nm) of Au was utilized from Johnson et al.[92] To generate the geometry of the Au NP clusters, we wrote a Python code that specifies the monomer radius, the length of the linear clusters of the Au NPs, and the interparticle gap distance, so as to generate input files. The following code is posted to GitHub in a public repository at https://github.com/KopelmanLab. Lastly, the effective radius is computed by

$$r_{\text{eff}} = (n(r_{\text{monomer}})^3)^{1/3} \tag{1}$$

Here r_{eff} is the effective radius, n is the length (number of units) of the linear clusters, and r_{monomer} is the radius of an Au NP monomer (10 nm).

Of particular importance for the discrete dipole computations is the number of dipoles per nanometer (dpnm) in the input geometry.[93,94] Previous studies have found that, above a 1 dpnm resolution for nanosized objects, the generated spectra are minimally affected by dpnm increases.[94] Hence, within the main body of this paper, all spectra are generated from 1 dpnm geometries.

Following the DDSCAT computations, UV−vis spectra were generated based on the simulated DDA extinction spectra and the experimentally measured mass distributions (TEM distributions) of the synthesized gold nanochains. Supporting Information Figure S12 shows a summary of the steps required for this process. In brief, a weighted linear combination of the DDA-computed spectra for linear clusters of Au NPs was taken with respect to each oligomer's percent frequency from the experimental TEM distribution. For every element (i.e., dimer, trimer, etc.) within the computed DDA linear combination set, the incoming light (k vector) x, y, z orientational contribution to the extinction spectra was averaged with equal weight (light is unpolarized along each orientation). Furthermore, due to the "resolution" of DDSCAT (using a 1 dpnm computation can only yield output for integer spacing), noninteger gap distance extinction spectra were interpolated using the 1.00, 2.00, and 3.00 nm computed extinction spectra (index data) at each wavelength (350−800 nm) from second order polynomial fitting. The interpolator model (polynomial reproducibility) was verified to be an exemplary method across the visible spectra (350 nm−800 nm), as the interpolated gap spectra are continuous, with no aberrant features and exhibiting the expected red-shifting of the longitudinal SPR as the gap distance narrows along both the x and the yz axes (Supporting Figure S13A−D). To fit the computed extinction spectra to the experimental extinction spectra, the computed extinction at 350 nm was used as a scale value (350 nm experimental extinction magnitude/350 nm computed extinction magnitude), and this scalar was multiplied across all wavelengths. The 350 nm value was chosen because it lies in a highly computationally predictable region for the DDA (away from the peak and areas sensitive to SPR). The mean squared error of the computed optical extinction spectra of the ensemble average was determined using gap distances ranging from 0.8 to 2.0 nm, with 0.05 nm resolution. The mean squared error (MSE) is defined as

$$\text{MSE} = \frac{\sum (n_{\text{theoretical}} - n_{\text{sample}})^2}{n} \tag{2}$$

where $n_{\text{theoretical}}$ is the value of the theoretical point (i.e., simulated "y") at value "x", n_{sample} is the value of the sample point (i.e., experimental "y") at the same "x", and n is the total number of theoretical samples evaluated in the sum.

4.8. Conjugation of RGD Peptides onto Au Nanochains. RGD peptides are well-known to bind preferentially to the $\alpha v\beta 3$ integrin proteins, which are overexpressed on the surface of most types of cancer cells.[95] Therefore, we chose to conjugate them onto gold nanochains for obtaining cancer cell-targeting conjugates. Within the five gold nanochain samples fabricated, the samples with longitudinal SPR at 640 nm were selected for this conjugation, and the conjugation was done by adding 12 μL of RGD peptide solution, with a concentration of 1 mM, to a 10 mL sample of gold nanochain with an optical density (OD) of 1 at 640 nm. The resultant solutions were allowed to stand for 2 h at room temperature, to ensure a sufficient conjugation of RGD peptides onto the unoccupied surfaces of the gold nanochains. The final solution was transferred into a 15 mL centrifugal tube and centrifuged at 1000g for 0.5 h. After removing the supernatant, the final OD of the RGD peptide-conjugated colloidal gold nanochains was adjusted to 10 by resuspending the NP pellet with 4 mM borate buffer (pH 8.2) containing 5 mg/mL BSA.

4.9. Human HeLa Cell Culture. The Human HeLa 229 cell line was selected for our study and was cultured according to the following protocol. (1) A total of 6 mL of human HeLa 229 cells in the logarithmic growth phase (American Type Culture Collection) at a density of 1×10^4 cells/mL, prepared in Dulbecco's modified Eagle medium (DMEM 11995) supplemented with 10% fetal bovine serum (FBS) and 1% penicillin-streptomycin, were first seeded into a BD Falcon Primaria tissue culture dish (100 mm × 20 mm) and were cultured aseptically at 37 °C and 5% CO_2 in a humidified incubator. (2) Cells were allowed to grow to at least 70% confluence in a 100 mm × 20 mm Petri dish. At the end of incubation, the culture medium was gently aspirated and then the cells were washed twice with 5 mL of Dulbecco's phosphate buffered saline (DPBS). (3) After their careful washing with DPBS, the cell culture was passaged, by incubating the cells with a 1 mL of 0.05% Trypsin-EDTA solution at 37 °C, until the cells attained a rounded morphology, followed by resuspension of the detached cells, by adding 4 mL of DMEM supplemented with 10% FBS and 1% penicillin-streptomycin, and centrifugation for 5 min at 500g. (4) Following the centrifugation, trypsin and DPBS were aspirated, and then the cell pellets were resuspended, by adding 3 mL of clear cell culture medium of DMEM without 10% FBS. (5) A total of 1 mL of the suspension of the cells from step 4 was replated into a 35 mm Petri dish, and then the cells were cultured for an additional 24 h at 37 °C and 5% CO_2 in a humidified incubator, thus allowing the cells to attach to the surface of

https://doi.org/10.1021/acs.chemmater.1c00336
Chem. Mater. 2021, 33, 2913−2928

a new Petri dish, prior to initiating treatment with the RGD peptide-conjugated gold nanochains.

4.10. Cellular Incubation with RGD Peptide-Conjugated Gold Nanochains. The following procedure was used to incubate Human HeLa 229 cells with RGD peptide-conjugated gold nanochains. (1) A stock solution of RGD-conjugated gold nanochains was mixed with Dulbecco's modified Eagle medium (DMEM 11995) without 10% fetal bovine serum (FBS), to achieve a new suspension of gold nanochains with an OD of 1 at the longitudinal SPR. (2) A 35 mm Petri dish containing the HeLa cells designated for an imaging test was aspirated of its original culture medium, which was followed by washing the cells twice with 1 mL of Dulbecco's phosphate buffered saline (DPBS). (3) Thereafter, a 1 mL suspension of RGD-conjugated gold nanochains from step 1 was added to the cells, and the cells were incubated for 12 h at 37 °C and 5% CO_2 in a humidified incubator, for allowing cellular uptake of the nanochains conjugates. (4) At the end of incubation, cells were washed with 1 mL of 1× PBS buffer, three times, to remove free gold nanochain conjugates in the solution. (5) The cells were fixed onto a Petri dish by adding 0.5 mL of fresh 4% paraformaldehyde in PBS for 15 min, followed by washing the cells three times with 1 mL 1× PBS buffer. (6) Finally, 1 mL of 1× PBS buffer was added to the Petri dish, and the cells were stored at 4 °C before the optical imaging analysis. To demonstrate the targeting efficacy and nanochain enhancement of the dark-field scattering, nontargeted controls of Au monomers and Au nanochains (with no surface attached RGD peptide) were incubated in HeLa cells, in addition to the RGD-conjugated Au monomers following the above protocol at identical incubation masses.

4.11. Dark-Field Light Scattering Imaging. The dark-field light scattering images were recorded using an inverted Nikon Epiphot 200 microscope equipped with an incandescent tungsten-halogen lamp (100 W) as a white light source. In order to acquire high-quality images, a high numerical aperture (NA > 0.55) is necessary. Therefore, a Nikon long working distance (f = 8 mm) 50× air immersion objective lens, with a numerical aperture of 0.55, was used to focus the incident light from the tungsten−halogen lamp onto the samples and also to collect only the scattered light from the samples. The dark-field light scattering pictures of the cells were captured by using a Nikon digital sight DS-Fi1 camera with an exposure time of 2 s. Under this dark-field light scattering microscope, intense colors of orange should be clearly seen to spread out in the human HeLa 229 cells, due to the intense light scattering of the internalized gold nanochains with an longitudinal SPR at 640 nm.

4.12. Cell Toxicity Experiments (MTT). The MTT (3-(4,5-dimethylthiazol-2-yl)-2,5-diphenyltetrazolium bromide) assay is employed as a way of measuring whether any stress is placed on the cells by being in the presence of the nanochains. By use of a 96-well plate, 5000 cells (HeLa, MDA-MB-231, BE(2)-C) were plated onto each well in 100 μL of Dulbecco's modified Eagle media of pH 7.4 (DMEM). The cells were incubated for 24 h, to ensure adhesion to the plate. For each cell line, a gold nanochain sample with longitudinal SPR at 640 nm was added to five wells, at mass concentrations of 0.025, 0.05, 0.125, and 0.25 mg/mL, with an adjusted volume of 200 μL for all wells. A control sample was made for each cell line, without any NP treatment. After an additional 24 h of incubation, 20 μL of a 0.5 mg/mL solution of the MTT dye in PBS was added to each well. After 3 h, the media were removed and replaced with 200 μL of dimethyl sulfoxide (DMSO). The plate was transferred to an Anthos 2010 plate reader and scanned at 550 nm excitation. To calculate the viability, the raw data for each nanochain mass concentration were averaged (n = 5), to reduce random error. The percent viability was normalized by dividing the average values for each nanochain mass concentration by the control average value. Error bars were determined from the compound standard deviation of the five trials for each sample.

■ ASSOCIATED CONTENT

Supporting Information

The Supporting Information is available free of charge at https://pubs.acs.org/doi/10.1021/acs.chemmater.1c00336.

Self-assembled Au nanobead chains with 705 nm and 710 longitudinal SPR; high-resolution TEM images of the nanochains; shelf life of the Au nanochains monitored through UV−vis; TEM images of nanochain batch to demonstrate intraparticle reproducibility; individual nanochain processing through CellProfiler; CellProfiler accuracy evaluated for intensity threshold classification; percent of unbranched chains under $1/m$, $1/m^{1.5}$, and $1/m^2$ diffusion dependent Monte Carlo simulations for various simulated sticking ratios (SSRs); nontargeted (no RGD conjugation) Au monomer and Au nanobead dark field controls; computed scattering enhancement per nanosphere of 590−640 nm longitudinal SPR nanochains under excitation from a tungsten halogen (500−700 nm excitation) lamp compared to a 20 nm Au monomer; nanoparticle diameter increase based on the molar ratio of CALNN peptide to Au monomer; DDSCAT pipeline for acquiring extinction, absorption, and scattering spectra; and interpolated DDA output spectra for trimers and a 15-mer between 0.8 to 3.0 nm (PDF)

Monte Carlo movie showing the simulated growth process for the 640 nm longitudinal SPR sample ($1/m^{1.5}$ diffusion dependence) (AVI)

Monte Carlo movie showing the simulated growth process for the 640 nm longitudinal SPR sample ($1/m^2$ diffusion dependence) (AVI)

■ AUTHOR INFORMATION

Corresponding Authors

Raoul Kopelman − *Department of Chemistry, University of Michigan, Ann Arbor, Michigan 48109, United States;* orcid.org/0000-0002-7770-8272; Email: kopelman@umich.edu

Wei Qian − *Department of Chemistry, University of Michigan, Ann Arbor, Michigan 48109, United States; IMRA America, Inc., Ann Arbor, Michigan 48105, United States;* Email: wqian@imra.com

Panos Argyrakis − *Department of Physics, Aristotle University of Thessaloniki, Thessaloniki 54124, Greece;* Email: panos@auth.gr

Authors

Alan McLean − *Department of Chemistry, University of Michigan, Ann Arbor, Michigan 48109, United States;* orcid.org/0000-0002-7226-7076

Michael Kanetidis − *Department of Physics, Aristotle University of Thessaloniki, Thessaloniki 54124, Greece*

Tarun Gogineni − *Department of Chemistry, University of Michigan, Ann Arbor, Michigan 48109, United States*

Rahil Ukani − *Department of Chemistry, University of Michigan, Ann Arbor, Michigan 48109, United States*

Ryan McLean − *Department of Chemistry, University of Michigan, Ann Arbor, Michigan 48109, United States*

Alexander Cooke − *Department of Chemistry, University of Michigan, Ann Arbor, Michigan 48109, United States*

Inbal Avinor − *Department of Chemistry, University of Michigan, Ann Arbor, Michigan 48109, United States*

Bing Liu − *IMRA America, Inc., Ann Arbor, Michigan 48105, United States*

Complete contact information is available at: https://pubs.acs.org/10.1021/acs.chemmater.1c00336

Notes

The authors declare no competing financial interest.

■ ACKNOWLEDGMENTS

The authors acknowledge the National Institutes of Health for funding support (R01CA186769). We acknowledge Dr. Tao Ma from the University of Michigan North Campus Center for Materials Characterization for the high-resolution TEM image collection.

■ REFERENCES

(1) Huang, X.; El-Sayed, M. A. Gold Nanoparticles: Optical Properties and Implementations in Cancer Diagnosis and Photothermal Therapy. *J. Adv. Res.* **2010**, *1* (1), 13−28.
(2) Wang, L.; Hasanzadeh Kafshgari, M.; Meunier, M. Optical Properties and Applications of Plasmonic-Metal Nanoparticles. *Adv. Funct. Mater.* **2020**, *30* (51), 2005400.
(3) Chen, Y.; Wu, H.; Li, Z.; Wang, P.; Yang, L.; Fang, Y. The Study of Surface Plasmon in Au/Ag Core/Shell Compound Nanoparticles. *Plasmonics* **2012**, *7* (3), 509−513.
(4) Bai, X.; Wang, Y.; Song, Z.; Feng, Y.; Chen, Y.; Zhang, D.; Feng, L. The Basic Properties of Gold Nanoparticles and Their Applications in Tumor Diagnosis and Treatment. *Int. J. Mol. Sci.* **2020**, *21* (7), 2480.
(5) Boisselier, E.; Astruc, D. Gold Nanoparticles in Nanomedicine: Preparations, Imaging, Diagnostics, Therapies and Toxicity. *Chem. Soc. Rev.* **2009**, *38* (6), 1759−1782.
(6) Chemla, Y.; Betzer, O.; Markus, A.; Farah, N.; Motiei, M.; Popovtzer, R.; Mandel, Y. Gold Nanoparticles for Multimodal High-Resolution Imaging of Transplanted Cells for Retinal Replacement Therapy. *Nanomedicine* **2019**, *14* (14), 1857−1871.
(7) Song, J.; Qu, J.; Swihart, M. T.; Prasad, P. N. Near-IR Responsive Nanostructures for Nanobiophotonics: Emerging Impacts on Nanomedicine. *Nanomedicine* **2016**, *12* (3), 771−788.
(8) Zhao, Y.; Huang, Y.; Zhu, H.; Zhu, Q.; Xia, Y. Three-in-One: Sensing, Self-Assembly, and Cascade Catalysis of Cyclodextrin Modified Gold Nanoparticles. *J. Am. Chem. Soc.* **2016**, *138* (51), 16645−16654.
(9) Qin, L.; Zeng, G.; Lai, C.; Huang, D.; Xu, P.; Zhang, C.; Cheng, M.; Liu, X.; Liu, S.; Li, B.; Yi, H. Gold Rush" in Modern Science: Fabrication Strategies and Typical Advanced Applications of Gold Nanoparticles in Sensing. *Coord. Chem. Rev.* **2018**, *359*, 1−31.
(10) Alim, S.; Vejayan, J.; Yusoff, M. M.; Kafi, A. K. M. Recent Uses of Carbon Nanotubes & Gold Nanoparticles in Electrochemistry with Application in Biosensing: A Review. *Biosens. Bioelectron.* **2018**, *121*, 125−136.
(11) Singh, P.; Pandit, S.; Mokkapati, V. R. S. S.; Garg, A.; Ravikumar, V.; Mijakovic, I. Gold Nanoparticles in Diagnostics and Therapeutics for Human Cancer. *Int. J. Mol. Sci.* **2018**, *19* (7), 1979.
(12) Lohse, S. E.; Murphy, C. J. Applications of Colloidal Inorganic Nanoparticles: From Medicine to Energy. *J. Am. Chem. Soc.* **2012**, *134* (38), 15607−15620.
(13) Lopes, T. S.; Alves, G. G.; Pereira, M. R.; Granjeiro, J. M.; Leite, P. E. C. Advances and Potential Application of Gold Nanoparticles in Nanomedicine. *J. Cell. Biochem.* **2019**, *120* (10), 16370−16378.
(14) Giljohann, D. A.; Seferos, D. S.; Daniel, W. L.; Massich, M. D.; Patel, P. C.; Mirkin, C. A. Gold Nanoparticles for Biology and Medicine. *Angew. Chem., Int. Ed.* **2010**, *49* (19), 3280−3294.
(15) Wang, J.; Zhu, G.; You, M.; Song, E.; Shukoor, M. I.; Zhang, K.; Altman, M. B.; Chen, Y.; Zhu, Z.; Huang, C. Z.; Tan, W. Assembly of Aptamer Switch Probes and Photosensitizer on Gold Nanorods for Targeted Photothermal and Photodynamic Cancer Therapy. *ACS Nano* **2012**, *6* (6), 5070−5077.
(16) Dreaden, E. C.; Alkilany, A. M.; Huang, X.; Murphy, C. J.; El-Sayed, M. A. The Golden Age: Gold Nanoparticles for Biomedicine. *Chem. Soc. Rev.* **2012**, *41* (7), 2740−2779.
(17) Ziegler, C.; Eychmüller, A. Seeded Growth Synthesis of Uniform Gold Nanoparticles with Diameters of 15−300 Nm. *J. Phys. Chem. C* **2011**, *115* (11), 4502−4506.
(18) Jacques, S. L. Optical Properties of Biological Tissues: A Review; Corrigendum. *Phys. Med. Biol.* **2013**, *58* (11), R37.
(19) Nguyen, V. P.; Qian, W.; Li, Y.; Liu, B.; Aaberg, M.; Henry, J.; Zhang, W.; Wang, X.; Paulus, Y. M. Chain-like Gold Nanoparticle Clusters for Multimodal Photoacoustic Microscopy and Optical Coherence Tomography Enhanced Molecular Imaging. *Nat. Commun.* **2021**, *12* (1), 34.
(20) Cao, J.; Sun, T.; Grattan, K. T. V. Gold Nanorod-Based Localized Surface Plasmon Resonance Biosensors: A Review. *Sens. Actuators, B* **2014**, *195*, 332−351.
(21) Rodríguez-Lorenzo, L.; Romo-Herrera, J. M.; Pérez-Juste, J.; Alvarez-Puebla, R. A.; Liz-Marzán, L. M. Reshaping and LSPR Tuning of Au Nanostars in the Presence of CTAB. *J. Mater. Chem.* **2011**, *21* (31), 11544−11549.
(22) Jiang, R.; Qin, F.; Liu, Y.; Ling, X. Y.; Guo, J.; Tang, M.; Cheng, S.; Wang, J. Colloidal Gold Nanocups with Orientation-Dependent Plasmonic Properties. *Adv. Mater.* **2016**, *28* (30), 6322−6331.
(23) Gharib, M.; Khalaf, M.; Afroz, S.; Feliu, N.; Parak, W. J.; Chakraborty, I. Sustainable Synthesis and Improved Colloidal Stability of Popcorn-Shaped Gold Nanoparticles. *ACS Sustainable Chem. Eng.* **2019**, *7* (11), 9834−9841.
(24) Lee, Y. H.; Lee, C. K.; Tan, B.; Rui Tan, J. M.; Phang, I. Y.; Ling, X. Y. Using the Langmuir-Schaefer Technique to Fabricate Large-Area Dense SERS-Active Au Nanoprism Monolayer Films. *Nanoscale* **2013**, *5* (14), 6404−6412.
(25) Alkilany, A. M.; Nagaria, P. K.; Hexel, C. R.; Shaw, T. J.; Murphy, C. J.; Wyatt, M. D. Cellular Uptake and Cytotoxicity of Gold Nanorods: Molecular Origin of Cytotoxicity and Surface Effects. *Small* **2009**, *5* (6), 701−708.
(26) Alkilany, A. M.; Shatanawi, A.; Kurtz, T.; Caldwell, R. B.; Caldwell, R. W. Toxicity and Cellular Uptake of Gold Nanorods in Vascular Endothelium and Smooth Muscles of Isolated Rat Blood Vessel: Importance of Surface Modification. *Small* **2012**, *8* (8), 1270−1278.
(27) Wan, J.; Wang, J. H.; Liu, T.; Xie, Z.; Yu, X. F.; Li, W. Surface Chemistry but Not Aspect Ratio Mediates the Biological Toxicity of Gold Nanorods in Vitro and in Vivo. *Sci. Rep.* **2015**, *5* (1), 11398.
(28) Barrow, S. J.; Funston, A. M.; Gómez, D. E.; Davis, T. J.; Mulvaney, P. Surface Plasmon Resonances in Strongly Coupled Gold Nanosphere Chains from Monomer to Hexamer. *Nano Lett.* **2011**, *11* (10), 4180−4187.
(29) Taylor, R. W.; Lee, T. C.; Scherman, O. A.; Esteban, R.; Aizpurua, J.; Huang, F. M.; Baumberg, J. J.; Mahajan, S. Precise Subnanometer Plasmonic Junctions for SERS within Gold Nanoparticle Assemblies Using Cucurbit[n]Uril "Glue". *ACS Nano* **2011**, *5* (5), 3878−3887.
(30) Willingham, B.; Link, S. Energy Transport in Metal Nanoparticle Chains via Sub-Radiant Plasmon Modes. *Opt. Express* **2011**, *19* (7), 6450.
(31) Slaughter, L. S.; Wang, L. Y.; Willingham, B. A.; Olson, J. M.; Swanglap, P.; Dominguez-Medina, S.; Link, S. Plasmonic Polymers Unraveled through Single Particle Spectroscopy. *Nanoscale* **2014**, *6* (19), 11451−11461.
(32) Halas, N. J.; Lal, S.; Chang, W. S.; Link, S.; Nordlander, P. Plasmons in Strongly Coupled Metallic Nanostructures. *Chem. Rev.* **2011**, *111* (6), 3913−3961.
(33) Tserkezis, C.; Herrmann, L. O.; Valev, V. K.; Baumberg, J. J.; Aizpurua, J. Optical Response of Threaded Chain Plasmons: From Capacitive Chains to Continuous Nanorods. *Opt. Express* **2014**, *22* (20), 23851.

(34) Lei, Y.; Yuan, M.; Yang, D.; Li, D. Unidirectional Light Scattering by up-down Janus Dimers Composed of Gold Nanospheres and Silicon Nanorods. *Opt. Commun.* **2019**, *435*, 362−366.
(35) Chang, W. S.; Willingham, B.; Slaughter, L. S.; Dominguez-Medina, S.; Swanglap, P.; Link, S. Radiative and Nonradiative Properties of Single Plasmonic Nanoparticles and Their Assemblies. *Acc. Chem. Res.* **2012**, *45* (11), 1936−1945.
(36) Pazos-Pérez, N.; Ni, W.; Schweikart, A.; Alvarez-Puebla, R. A.; Fery, A.; Liz-Marzán, L. M. Highly Uniform SERS Substrates Formed by Wrinkle-Confined Drying of Gold Colloids. *Chem. Sci.* **2010**, *1* (2), 174−178.
(37) Hooshmand, N.; Mousavi, H. S.; Panikkanvalappil, S. R.; Adibi, A.; El-Sayed, M. A. High-Sensitivity Molecular Sensing Using Plasmonic Nanocube Chains in Classical and Quantum Coupling Regimes. *Nano Today* **2017**, *17*, 14−22.
(38) Zuo, T.; Goldwyn, H. J.; Isaacoff, B. P.; Masiello, D. J.; Biteen, J. S. Rotation of Single-Molecule Emission Polarization by Plasmonic Nanorods. *J. Phys. Chem. Lett.* **2019**, *10* (17), 5047−5054.
(39) Lee, S. A.; Biteen, J. S. Spectral Reshaping of Single Dye Molecules Coupled to Single Plasmonic Nanoparticles. *J. Phys. Chem. Lett.* **2019**, *10* (19), 5764−5769.
(40) Dinish, U. S.; Song, Z.; Ho, C. J. H.; Balasundaram, G.; Attia, A. B. E.; Lu, X.; Tang, B. Z.; Liu, B.; Olivo, M. Single Molecule with Dual Function on Nanogold: Biofunctionalized Construct for in Vivo Photoacoustic Imaging and SERS Biosensing. *Adv. Funct. Mater.* **2015**, *25* (15), 2316−2325.
(41) Hatef, A.; Meunier, M. Plasma-Mediated Photothermal Effects in Ultrafast Laser Irradiation of Gold Nanoparticle Dimers in Water. *Opt. Express* **2015**, *23* (3), 1967.
(42) Grzelczak, M.; Vermant, J.; Furst, E. M.; Liz-Marzán, L. M. Directed Self-Assembly of Nanoparticles. *ACS Nano* **2010**, *4* (7), 3591−3605.
(43) Mayer, M.; Schnepf, M. J.; König, T. A. F.; Fery, A. Colloidal Self-Assembly Concepts for Plasmonic Metasurfaces. *Adv. Opt. Mater.* **2019**, *7* (1), 1800564.
(44) Zhang, D.; Gökce, B.; Barcikowski, S. Laser Synthesis and Processing of Colloids: Fundamentals and Applications. *Chem. Rev.* **2017**, *117* (5), 3990−4103.
(45) Ganjali, M.; Ganjali, M.; Vahdatkhah, P.; Marashi, S. M. B. Synthesis of Ni Nanoparticles by Pulsed Laser Ablation Method in Liquid Phase. *Procedia Mater. Sci.* **2015**, *11*, 359−363.
(46) Amendola, V.; Meneghetti, M. What Controls the Composition and the Structure of Nanomaterials Generated by Laser Ablation in Liquid Solution? *Phys. Chem. Chem. Phys.* **2013**, *15* (9), 3027−3046.
(47) Burke, D. J.; Lipomi, D. J. Green Chemistry for Organic Solar Cells. *Energy Environ. Sci.* **2013**, *6* (7), 2053−2066.
(48) Sylvestre, J. P.; Kabashin, A. V.; Sacher, E.; Meunier, M.; Luong, J. H. T. Stabilization and Size Control of Gold Nanoparticles during Laser Ablation in Aqueous Cyclodextrins. *J. Am. Chem. Soc.* **2004**, *126* (23), 7176−7177.
(49) Qian, W.; Murakami, M.; Ichikawa, Y.; Che, Y. Highly Efficient and Controllable PEGylation of Gold Nanoparticles Prepared by Femtosecond Laser Ablation in Water. *J. Phys. Chem. C* **2011**, *115* (47), 23293−23298.
(50) Shao, X.; Schnau, P.; Qian, W.; Wang, X. Quantitatively Understanding Cellular Uptake of Gold Nanoparticles via Radioactivity Analysis. *J. Nanosci. Nanotechnol.* **2015**, *15* (5), 3834−3838.
(51) Wu, P. H.; Onodera, Y.; Ichikawa, Y.; Rankin, E. B.; Giaccia, A. J.; Watanabe, Y.; Qian, W.; Hashimoto, T.; Shirato, H.; Nam, J. M. Targeting Integrins with RGD-Conjugated Gold Nanoparticles in Radiotherapy Decreases the Invasive Activity of Breast Cancer Cells. *Int. J. Nanomed.* **2017**, *12*, 5069−5085.
(52) Tian, C.; Qian, W.; Shao, X.; Xie, Z.; Cheng, X.; Liu, S.; Cheng, Q.; Liu, B.; Wang, X. Plasmonic Nanoparticles with Quantitatively Controlled Bioconjugation for Photoacoustic Imaging of Live Cancer Cells. *Adv. Sci.* **2016**, *3* (12), 1600237.
(53) Lévy, R.; Thanh, N. T. K.; Doty, R. C.; Hussain, I.; Nichols, R. J.; Schiffrin, D. J.; Brust, M.; Fernig, D. G. Rational and Combinatorial Design of Peptide Capping Ligands for Gold Nanoparticles. *J. Am. Chem. Soc.* **2004**, *126* (32), 10076−10084.
(54) Liang, X.; Wei, H.; Cui, Z.; Deng, J.; Zhang, Z.; You, X.; Zhang, X. E. Colorimetric Detection of Melamine in Complex Matrices Based on Cysteamine-Modified Gold Nanoparticles. *Analyst* **2011**, *136* (1), 179−183.
(55) Gukowsky, J. C.; Tan, C.; Han, Z.; He, L. Cysteamine-Modified Gold Nanoparticles as a Colorimetric Sensor for the Rapid Detection of Gentamicin. *J. Food Sci.* **2018**, *83* (6), 1631−1638.
(56) Yang, M.; Chen, G.; Zhao, Y.; Silber, G.; Wang, Y.; Xing, S.; Han, Y.; Chen, H. Mechanistic Investigation into the Spontaneous Linear Assembly of Gold Nanospheres. *Phys. Chem. Chem. Phys.* **2010**, *12* (38), 11850−11860.
(57) Carnegie, C.; Chikkaraddy, R.; Benz, F.; De Nijs, B.; Deacon, W. M.; Horton, M.; Wang, W.; Readman, C.; Barrow, S. J.; Scherman, O. A.; Baumberg, J. J. Mapping SERS in CB:Au Plasmonic Nanoaggregates. *ACS Photonics* **2017**, *4* (11), 2681−2686.
(58) Liao, J.; Zhang, Y.; Yu, W.; Xu, L.; Ge, C.; Liu, J.; Gu, N. Linear Aggregation of Gold Nanoparticles in Ethanol. *Colloids Surf., A* **2003**, *223* (1−3), 177−183.
(59) Gao, M. R.; Zhang, S. R.; Xu, Y. F.; Zheng, Y. R.; Jiang, J.; Yu, S. H. Self-Assembled Platinum Nanochain Networks Driven by Induced Magnetic Dipoles. *Adv. Funct. Mater.* **2014**, *24* (7), 916−924.
(60) Jia, H.; Bai, X.; Zheng, L. One-Step Synthesis and Assembly of Gold Nanochains Using the Langmuir Monolayer of Long-Chain Ionic Liquids and Their Applications to SERS. *CrystEngComm* **2012**, *14* (8), 2920−2925.
(61) Woehl, T. J.; Prozorov, T. The Mechanisms for Nanoparticle Surface Diffusion and Chain Self-Assembly Determined from Real-Time Nanoscale Kinetics in Liquid. *J. Phys. Chem. C* **2015**, *119* (36), 21261−21269.
(62) Lu, J.; Aabdin, Z.; Loh, N. D.; Bhattacharya, D.; Mirsaidov, U. Nanoparticle Dynamics in a Nanodroplet. *Nano Lett.* **2014**, *14* (4), 2111−2115.
(63) Woehl, T. J.; Park, C.; Evans, J. E.; Arslan, I.; Ristenpart, W. D.; Browning, N. D. Direct Observation of Aggregative Nanoparticle Growth: Kinetic Modeling of the Size Distribution and Growth Rate. *Nano Lett.* **2014**, *14* (1), 373−378.
(64) Verch, A.; Pfaff, M.; De Jonge, N. Exceptionally Slow Movement of Gold Nanoparticles at a Solid/Liquid Interface Investigated by Scanning Transmission Electron Microscopy. *Langmuir* **2015**, *31* (25), 6956−6964.
(65) Xing, S.; Tan, L. H.; Yang, M.; Pan, M.; Lv, Y.; Tang, Q.; Yang, Y.; Chen, H. Highly Controlled Core/Shell Structures: Tunable Conductive Polymer Shells on Gold Nanoparticles and Nanochains. *J. Mater. Chem.* **2009**, *19* (20), 3286−3291.
(66) Sánchez, V. M.; Martínez, E. D.; Martínez Ricci, M. L.; Troiani, H.; Soler-Illia, G. J. A. A. Optical Properties of Au Nanoparticles Included in Mesoporous TiO 2 Thin Films: A Dual Experimental and Modeling Study. *J. Phys. Chem. C* **2013**, *117* (14), 7246−7259.
(67) Albanese, A.; Chan, W. C. W. Effect of Gold Nanoparticle Aggregation on Cell Uptake and Toxicity. *ACS Nano* **2011**, *5* (7), 5478−5489.
(68) Zhao, L.; Kim, T. H.; Kim, H. W.; Ahn, J. C.; Kim, S. Y. Surface-Enhanced Raman Scattering (SERS)-Active Gold Nanochains for Multiplex Detection and Photodynamic Therapy of Cancer. *Acta Biomater.* **2015**, *20*, 155−164.
(69) Huang, X.; Jain, P. K.; El-Sayed, I. H.; El-Sayed, M. A. Plasmonic Photothermal Therapy (PPTT) Using Gold Nanoparticles. *Lasers Med. Sci.* **2008**, *23* (3), 217−228.
(70) Proetto, M. T.; Alexander, K.; Melaimi, M.; Bertrand, G.; Gianneschi, N. C. Cyclic (Alkyl)(Amino)Carbene (CAAC) Gold(I) Complexes as Chemotherapeutic Agents. *Chem. - Eur. J.* **2021**, *27* (11), 3772−3778.
(71) Korpanty, J.; Parent, L. R.; Gianneschi, N. C. Enhancing and Mitigating Radiolytic Damage to Soft Matter in Aqueous Phase Liquid-Cell Transmission Electron Microscopy in the Presence of Gold Nanoparticle Sensitizers or Isopropanol Scavengers. *Nano Lett.* **2021**, *21* (2), 1141−1149.

(72) Sylvestre, J. P.; Poulin, S.; Kabashin, A. V.; Sacher, E.; Meunier, M.; Luong, J. H. T. Surface Chemistry of Gold Nanoparticles Produced by Laser Ablation in Aqueous Media. *J. Phys. Chem. B* **2004**, *108* (43), 16864−16869.
(73) Kozlowski, R.; Ragupathi, A.; Dyer, R. B. Characterizing the Surface Coverage of Protein-Gold Nanoparticle Bioconjugates. *Bioconjugate Chem.* **2018**, *29* (8), 2691−2700.
(74) James, A. E.; Driskell, J. D. Monitoring Gold Nanoparticle Conjugation and Analysis of Biomolecular Binding with Nanoparticle Tracking Analysis (NTA) and Dynamic Light Scattering (DLS). *Analyst* **2013**, *138* (4), 1212−1218.
(75) Scott, A. W.; Garimella, V.; Calabrese, C. M.; Mirkin, C. A. Universal Biotin-PEG-Linked Gold Nanoparticle Probes for the Simultaneous Detection of Nucleic Acids and Proteins. *Bioconjugate Chem.* **2017**, *28* (1), 203−211.
(76) Jia, Y.; Yan, X.; Guo, X.; Zhou, G.; Liu, P.; Li, Z. One Step Preparation of Peptide-Coated Gold Nanoparticles with Tunable Size. *Materials* **2019**, *12* (13), 2107.
(77) Sharma, A. K.; Pandey, S.; Nerthigan, Y.; Swaminathan, N.; Wu, H. F. Aggregation of Cysteamine-Capped Gold Nanoparticles in Presence of ATP as an Analytical Tool for Rapid Detection of Creatine Kinase (CK-MM). *Anal. Chim. Acta* **2018**, *1024*, 161−168.
(78) Kamentsky, L.; Jones, T. R.; Fraser, A.; Bray, M. A.; Logan, D. J.; Madden, K. L.; Ljosa, V.; Rueden, C.; Eliceiri, K. W.; Carpenter, A. E. Improved Structure, Function and Compatibility for Cellprofiler: Modular High-Throughput Image Analysis Software. *Bioinformatics* **2011**, *27* (8), 1179−1180.
(79) Ribeiro, G. P.; Valotto, R. S.; de Oliveira, J. P.; Guimarães, M. C. C.; Lenz, D. An Inexpensive, Automated and Reproducible Method to Conduct Quality Control in Nanoparticles. *Chem. Pap.* **2020**, *74* (9), 2821−2824.
(80) Rottereau, M.; Gimel, J. C.; Nicolai, T.; Durand, D. Monte Carlo Simulation of Particle Aggregation and Gelation: I. Growth, Structure and Size Distribution of the Clusters. *Eur. Phys. J. E: Soft Matter Biol. Phys.* **2004**, *15* (2), 133−140.
(81) González, A.E; Martínez-López, F; Moncho-Jordá, A; Hidalgo-Álvarez, R Concentration Effects on Two- and Three-Dimensional Colloidal Aggregation. *Phys. A* **2002**, *314*, 235−245.
(82) Tolman, S.; Meakin, P. Off-lattice and hypercubic-lattice models for diffusion-limited in dimensionalities 2—8 aggregation. *Phys. Rev. A: At., Mol., Opt. Phys.* **1989**, *40* (1), 428−437.
(83) Oh, C.; Sorensen, C. M. Structure Factor of Diffusion-Limited Aggregation Clusters: Local Structure and Non-Self-Similarity. *Phys. Rev. E: Stat. Phys., Plasmas, Fluids, Relat. Interdiscip. Top.* **1998**, *57* (1), 784−790.
(84) Kanetidis, M.; Tsouchnika, M.; Argyrakis, P.; Kopelman, R. A Simple Model for Charged Particle Aggregation and Polarization. *Phys. A* **2019**, *528*, 121433.
(85) Vicsek, T. *Fractal Growth Phenomena*; World Scientific: 1992; DOI: 10.1142/1407.
(86) Meakin, P. Formation of Fractal Clusters and Networks by Irreversible Diffusion-Limited Aggregation. *Phys. Rev. Lett.* **1983**, *51* (13), 1119−1122.
(87) Meakin, P. Aggregation Kinetics. *Phys. Scr.* **1992**, *46* (4), 295−331.
(88) Bunde, A.; Havlin, S.; Nossal, R.; Stanley, H. E.; Weiss, G. H. On Controlled Diffusion-Limited Drug Release from a Leaky Matrix. *J. Chem. Phys.* **1985**, *83* (11), 5909−5913.
(89) Kosmidis, K.; Argyrakis, P.; Macheras, P. A Reappraisal of Drug Release Laws Using Monte Carlo Simulations: The Prevalence of the Weibull Function. *Pharm. Res.* **2003**, *20* (7), 988−995.
(90) Draine, B. T.; Flatau, P. J. Discrete-Dipole Approximation For Scattering Calculations. *J. Opt. Soc. Am. A* **1994**, *11* (4), 1491.
(91) Yurkin, M. A.; Hoekstra, A. G. The Discrete Dipole Approximation: An Overview and Recent Developments. *J. Quant. Spectrosc. Radiat. Transfer* **2007**, *106* (1−3), 558−589.
(92) Johnson, P. B.; Christy, R. W. Optical Constant of the Nobel Metals. *Phys. L Re View B* **1972**, *6* (12), 4370−4379.
(93) Amendola, V.; Bakr, O. M.; Stellacci, F. A Study of the Surface Plasmon Resonance of Silver Nanoparticles by the Discrete Dipole Approximation Method: Effect of Shape, Size, Structure, and Assembly. *Plasmonics* **2010**, *5* (1), 85−97.
(94) Kealley, C. S.; Cortie, M. B. A Computational Exploration of the Color Gamut of Nanoscale Hollow Scalene Ellipsoids of Ag and Au. *Plasmonics* **2010**, *5* (1), 37−43.
(95) Muhamad, N.; Plengsuriyakarn, T.; Na-Bangchang, K. Application of Active Targeting Nanoparticle Delivery System for Chemotherapeutic Drugs and Traditional/Herbal Medicines in Cancer Therapy: A Systematic Review. *Int. J. Nanomed.* **2018**, *13*, 3921−3935.